

# Controls of the Foreland-Deformation Pattern in the Orogen-Foreland Shortening System: Constraints from High-Resolution Geodynamic Models

Sibiao Liu<sup>1,1</sup>, Stephan V. Sobolev<sup>2,2</sup>, Andrey Y. Babeyko<sup>2,2</sup>, and Michaël Vincent Pons-Rallo<sup>3,3</sup>

<sup>1</sup>GEOMAR Helmholtz Centre for Ocean Research Kiel

<sup>2</sup>Helmholtz Centre Potsdam GFZ German Research Centre for Geosciences

<sup>3</sup>Helmholtz Centre Potsdam, GFZ German Research Science for Geosciences

November 30, 2022

## Abstract

Controls on the deformation pattern (shortening mode and tectonic style) of orogenic forelands during lithospheric shortening remain poorly understood. Here, we use high-resolution 2D thermomechanical models to demonstrate that orogenic crustal thickness and foreland lithospheric thickness significantly control the shortening mode in the foreland. Pure-shear shortening occurs when the orogenic crust is not thicker than the foreland crust or thick, but the foreland lithosphere is thin ( $< 70\text{-}80$  km, as in the Puna foreland case). Conversely, simple-shear shortening, characterized by foreland underthrusting beneath the orogen, arises when the orogenic crust is much thicker. This thickened crust results in high gravitational potential energy in the orogen, which triggers the migration of deformation to the foreland under further shortening. Our models present fully thick-skinned, fully thin-skinned, and intermediate tectonic styles in the foreland. The first tectonic forms in a pure-shear shortening mode whereas the others require a simple-shear mode and the presence of thick ( $> \sim 4$  km) sediments that are mechanically weak (friction coefficient  $< \sim 0.05$ ) or weakened rapidly during deformation. The formation of fully thin-skinned tectonics in thick and weak foreland sediments, as in the Subandean Ranges, requires the strength of the orogenic upper lithosphere to be less than one-third as strong as that of the foreland upper lithosphere. Our models successfully reproduce foreland deformation patterns in the Central and Southern Andes and the Laramide province.

1 **Controls of the Foreland Deformation Pattern in the Orogen-Foreland Shortening**  
2 **System: Constraints from High-Resolution Geodynamic Models**

3

4 Sibiao Liu<sup>1, 2, 3</sup>, Stephan V. Sobolev<sup>2,3</sup>, Andrey Y. Babeyko<sup>2</sup>, Michael Pons<sup>2, 3</sup>

5 <sup>1</sup>GEOMAR Helmholtz Centre for Ocean Research Kiel, Kiel, Germany

6 <sup>2</sup>German Research Center for Geosciences GFZ, Potsdam, Germany

7 <sup>3</sup>Institute of Earth and Environmental Science, University of Potsdam, Potsdam, Germany

8

9 Corresponding author: S. Liu (sliu@geomar.de)

10

11 **Key Points:**

- 12
- Thicknesses of the orogenic crust and the foreland lithosphere control the foreland  
13 shortening mode (pure-shear or simple-shear).
  - Foreland weak sediments and the upper lithosphere of the weaker orogen control the  
14 foreland tectonic style (thin-skinned or thick-skinned).
  - High-resolution geodynamic models successfully reproduce foreland deformation  
15 patterns in several natural orogen-foreland shortening systems.  
16  
17

## 18 **Abstract**

19 Controls on the deformation pattern (shortening mode and tectonic style) of orogenic  
20 forelands during lithospheric shortening remain poorly understood. Here, we use high-  
21 resolution 2D thermomechanical models to demonstrate that orogenic crustal thickness and  
22 foreland lithospheric thickness significantly control the shortening mode in the foreland. Pure-  
23 shear shortening occurs when the orogenic crust is not thicker than the foreland crust or thick,  
24 but the foreland lithosphere is thin ( $< 70\text{-}80$  km, as in the Puna foreland case). Conversely,  
25 simple-shear shortening, characterized by foreland underthrusting beneath the orogen, arises  
26 when the orogenic crust is much thicker. This thickened crust results in high gravitational  
27 potential energy in the orogen, which triggers the migration of deformation to the foreland  
28 under further shortening. Our models present fully thick-skinned, fully thin-skinned, and  
29 intermediate tectonic styles in the foreland. The first tectonics forms in a pure-shear  
30 shortening mode whereas the others require a simple-shear mode and the presence of thick ( $>$   
31  $\sim 4$  km) sediments that are mechanically weak (friction coefficient  $< \sim 0.05$ ) or weakened  
32 rapidly during deformation. The formation of fully thin-skinned tectonics in thick and weak  
33 foreland sediments, as in the Subandean Ranges, requires the strength of the orogenic upper  
34 lithosphere to be less than one-third as strong as that of the foreland upper lithosphere. Our  
35 models successfully reproduce foreland deformation patterns in the Central and Southern  
36 Andes and the Laramide province.

## 37 **1 Introduction**

38 In the orogen-foreland shortening system, pure- and simple-shear are two common  
39 shortening modes in foreland deformation belts. The pure-shear shortening mode is  
40 characterized by a vertically quasi-homogeneous thickening of the foreland crust. In contrast,  
41 the foreland lithosphere underthrusts beneath the orogen along a low-angle detachment fault  
42 in the simple-shear mode. During shortening, crustal-scale deformation in the foreland forms  
43 either shallow thin-skinned or deep thick-skinned tectonics (e.g., Dahlen, 1990, Lacombe &  
44 Bellahsen, 2016; Pfiffner, 2017). In the former, the sedimentary cover overlies the almost  
45 undeformed basement along a shallow décollement fault, while faults reach down into the  
46 basement in the latter. These different foreland deformation patterns (i.e., shortening mode  
47 and tectonic style) are generally found in natural orogens, for example, in the Central-  
48 Southern Andes (e.g., Ramos et al., 2004; Giambiagi et al., 2011; Mescua et al., 2016),  
49 Southern Canadian Rockies (e.g., Price, 1981; Stockmal et al., 2007), Laramide Rocky  
50 Mountains (e.g., DeCelles, 2004; Yonkee & Weil, 2015), Taiwan and Alps (e.g., Lacombe &

51 Mouthereau, 2002; Mouthereau & Lacombe, 2006; Bellahsen et al., 2014; Lacombe &  
52 Bellahsen, 2016; Pfiffner, 2016), and the Zagros (e.g., Mouthereau et al., 2006, 2007; Jammes  
53 & Huismans, 2012; Mouthereau et al., 2012; Nilfouroushan et al., 2013).

54         The transition between the two shortening modes and how thin-skinned and thick-  
55 skinned tectonics interact are unclear. Previous studies have suggested that the foreland  
56 deformation pattern is related to the contrast in lithospheric strength between the orogen and  
57 its foreland (e.g., Babeyko et al., 2006; Jammes & Huismans, 2012; Mouthereau et al., 2013;  
58 Erdős et al., 2015). For instance, Jammes and Huismans (2012) demonstrated that the  
59 deformation of a weak orogen accommodates a few thick-skinned crustal-scale thrusts with  
60 moderate displacement and distributed crustal thickening, as observed in the Zagros. This  
61 weakness may result from its mechanically weak composition (i.e., low viscosity) or high  
62 geothermal gradient (Nilfouroushan et al., 2013). The orogenic deformation is also related to  
63 the foreland lithospheric strength through dependence on the age of the lithosphere during  
64 shortening (Mouthereau et al., 2013). A thin-skinned thrust zone will form in the orogen if its  
65 foreland is old, cold, and strong. Erdős et al. (2015) found that synorogenic sedimentation on  
66 the external parts of an orogen may provide first-order control on its basement deformation  
67 style. In sediment-starved orogens, such as the Southern Urals case, thick-skinned  
68 deformation is mainly located in the orogenic core. When the orogen is sediment-loaded, such  
69 as the Swiss Alps, this basement-involved structure appears in the axial zone and its foreland.  
70 Moreover, a sudden drop in the mechanical strength of foreland sediments can lead to a shift  
71 of the shortening mode from pure- to simple-shear and the formation of thin-skinned structure  
72 in the foreland (Babeyko et al., 2006).

73         However, these studies mainly focused on structural styles of the orogen; the foreland  
74 deformation pattern has received less attention. In particular, the exact nature of variations in  
75 lithospheric strength and sediment weakening affecting the evolution of foreland deformation  
76 is still not well understood. In addition, the question of whether controlled factors from these  
77 studies can be applied to explain the deformation patterns in other forelands remains open.  
78 The above-cited models also did not explore more details of the foreland deformation features  
79 (e.g., the fault direction) due to the lack of necessary numerical resolution. Recent progress in  
80 numerical modeling techniques extends this research to higher-resolution lithospheric models,  
81 which is the subject of the current study.

82         The long-term evolution of continental lithospheric strength is primarily controlled by  
83 its composition and temperature, which strongly depend on depth, i.e., the lithospheric  
84 thickness and the crustal thickness (e.g., Kusznir & Park, 1986; Ellis, 1988; Cloetingh &

85 Burov, 1996). The lithosphere can be stronger due to lithospheric thickening and/or crustal  
86 thinning (**Figure A1**). The composition, fluid content (degree of hydration), magmatism, and  
87 thermal/structural inheritance also influence on the lithospheric strength (e.g., Kohlstedt et al.,  
88 1995; Burov & Watt, 2006; Burov, 2011; Mouthereau et al., 2013; Erdős et al., 2015). For  
89 example, the subduction process can weaken the foreland lithosphere in a subduction-  
90 dominated orogeny by a high degree of hydration or a hot thermal structure. In this study, we  
91 addressed the key (although certainly not all) controlling factors: thickness of the thermal  
92 lithosphere and thickness of the crust. Together, these two factors also automatically  
93 determine the partitioning of the lithosphere into the crust and mantle lithosphere, thus also  
94 taking into account the effect of the composition and at least partially.

95         Weakening of foreland sediments can facilitate the initiation of foreland crustal  
96 underthrusting below the orogen, thereby promoting the formation of simple-shear shortening  
97 (Babeyko & Sobolev, 2005). Therefore, the sedimentary strength should also be considered in  
98 the development of the foreland deformation pattern. Although the strength of the lithosphere  
99 already includes the top sedimentary strength, the latter has a limited effect on the former. On  
100 the one hand, although the sedimentary cover is approximately 8 km thick or more (Laske et  
101 al., 2013), its thickness is still less than one-tenth of a typical continental lithospheric  
102 thickness (~100-200 km thick). Accordingly, changes in sedimentary strength due to  
103 thickness variations have little effect on the strength of the entire lithosphere. On the other  
104 hand, the shallow frictional brittle strength ( $\sigma_B$  in Equation 6) in the first few kilometers of  
105 the crust (1-14 km), which depends highly on pressure rather than compositions (Byerlee,  
106 1978), has less influence on the lithospheric strength than the deep ductile strength (**Figure**  
107 **A1**). Thus, changes in the sedimentary strength due to different compositions hardly affect the  
108 brittle strength and cause fewer changes in the entire lithospheric strength. In other words, the  
109 change in the strength of foreland sediments does not significantly change the strength of the  
110 lithosphere. However, it is important for the deformation evolution of the shallow crust of the  
111 foreland. Therefore, these two factors should be considered separately regarding the influence  
112 on the deformation pattern of the foreland crust.

113         The friction coefficient of the sediment is another factor other than thickness that  
114 controls its strength (see **Appendix**). It has a wide range of values from  $> 0.8$  to  $< 0.05$ ,  
115 depending on temperature, composition, pore-fluid pressure, and asperities along the fault  
116 surface (Hassani et al., 1997). If sedimentary rocks contain sufficient clay minerals such as  
117 montmorillonite or vermiculite (Byerlee, 1978), the friction value can be as low as 0.1. The  
118 value can be further decreased to 0.015, which is predicted for subduction channels in some

119 geodynamic models (Sobolev et al., 2006). A reduction in the friction coefficient can decrease  
120 the yield strength of the rock, thereby accelerating its failure. The physical nature of potential  
121 frictional weakening in foreland sediments remains controversial. This may result from high  
122 pore-fluid pressure (lowering the effective confining stress) due to rapid hydrocarbon  
123 generation (Cobbold et al., 2004 and reference therein), an increase in precipitation (e.g.,  
124 Strecker et al., 2007), or compaction under strong compression in the foreland (e.g., Babeyko  
125 & Sobolev, 2005). Since we are concerned with crustal-scale deformation in the foreland, the  
126 exact origin of the sedimentary friction drop is not discussed here.

127 In this study, we first examine how different factors influence the lithospheric strength  
128 of the orogen and its foreland (factors: lithospheric thickness and crustal thickness). We also  
129 examine the mechanical strength of foreland sediments (factors: effective friction coefficient  
130 of sediments and sedimentary thickness). Then, we systematically investigate how these  
131 parameters control the foreland deformation pattern during orogen-foreland shortening.  
132 Finally, we apply model results to natural orogen-foreland systems such as the Central-  
133 Southern Andes and the Laramide province.

## 134 **2 Numerical Model Description**

### 135 **2.1 Method and Model Geometry**

136 We use the highly scalable parallel code LaMEM (Lithosphere and Mantle Evolution  
137 Model; Kaus et al., 2016) that solves three geodynamic conservation equations (see  
138 **Appendix**) to govern material deformation. The model contains two structural domains - the  
139 orogen and its foreland - 400 km wide and 400 km deep. As we are interested in the  
140 deformation of the foreland crust, we plot our modeling results in the zoomed-in area in the  
141 top 60 km of the model (dashed gray rectangle in **Figure 1**) with a horizontal distance  
142 between 50 km and 330 km. By doing so, we suppose the effect of side boundary conditions  
143 on the modeling results in this area minimized (see **Figure S1** in the supporting information,  
144 showing that the boundary effects on our zoom-in models can be negligible).

145 The lithospheric thicknesses of the orogen and its foreland in the model vary from 60  
146 km to 200 km. **Figure 1** shows a 60-km-thick lithospheric strength profile. This is an example  
147 of a thin and weak orogenic lithosphere due to lithosphere delamination (e.g., Kay & Kay,  
148 1993). The felsic crust in the foreland is 24 km thick and has a sedimentary cover of varying  
149 thickness (0-8 km). Below it, there is a 12-km-thick mafic crust. In contrast, the thickness of  
150 the orogenic crust varies between 36 km and 70 km. A thick orogenic crust could be produced  
151 by tectonic shortening during orogenesis in natural orogens such as the Tibetan Plateau and

152 the Central Andes (e.g., Holt & Wallace, 1990; Ramos et al., 2004). The entire model domain  
153 has a uniform 500-m-high grid resolution, ensuring that the deformation in such a thin  
154 sedimentary layer is tracked correctly.

## 155 **2.2 Material Properties and Boundary Conditions**

156 The material thermomechanical properties are given in **Table 1**. All materials contain  
157 a viscoelastoplastic rheology, where diffusion and dislocation viscous creep regimes are used  
158 to mimic ductile deformation. The laboratory-derived flow laws of wet quartzite (Qtz<sub>wet</sub>;  
159 Gleason & Tullis, 1995), dry Maryland diabase (MD<sub>dry</sub>; Mackwell et al., 1998), and wet/dry  
160 olivine (Ol<sub>wet</sub>/Ol<sub>dry</sub>; Hirth & Kohlstedt, 2003) are used for the felsic crust and its sedimentary  
161 cover, the mafic crust, and the lithospheric mantle/asthenosphere, respectively. The felsic  
162 crust undergoes frictional-plastic strain-softening through a friction coefficient decrease from  
163 0.58 to 0.1 over the accumulated strain of 0.5 to 1.5, including the friction angle from 30° to  
164 6° and the cohesion from 20 MPa to 1 MPa (**Table 1**). This follows values used in previous  
165 geodynamic models (e.g., Sobolev et al., 2006; Erdős et al., 2015).

166 The values of thermal parameters are within the range expected for crustal and mantle  
167 materials (e.g., Sobolev et al., 2006; Barrionuevo et al., 2021). Radiogenic heat production is  
168 1.0  $\mu\text{W m}^{-3}$  in the felsic crust and 0.3  $\mu\text{W m}^{-3}$  in the mafic crust. The thermal conductivity  
169 increases from 2.5  $\text{W m}^{-1} \text{K}^{-1}$  in the crust to 3.3  $\text{W m}^{-1} \text{K}^{-1}$  in the mantle. Material density is  
170 temperature-dependent (**Table 1**). The continental felsic crust has a reference density of 2800  
171  $\text{kg m}^{-3}$  at room temperature to reflect a more felsic (silica-rich) composition than the mafic  
172 crust below. The density of the sediments is 300  $\text{kg m}^{-3}$  less than the density of continental  
173 felsic rocks at the same temperature. The reference density of the mantle (3300  $\text{kg m}^{-3}$ ) is  
174 consistent with the density of the fertile lithospheric mantle (Poudjom Djomani et al., 2001).

175 **Figure 1** shows the initial thermal-mechanical boundary condition. The initial  
176 temperature setting of the model is divided into two steps. It first increases linearly with depth  
177 from 0 °C at the surface to 1328-1380 °C at the lithosphere base depending on the lithospheric  
178 thickness. It then rises adiabatically to 1460 °C at the bottom boundary. The thermal gradient  
179 at side boundaries is taken to be zero, which means no horizontal heat flux. We used the  
180 “sticky air” top boundary with the free surface stabilization approach (Kaus et al., 2010). This  
181 10-km-thick layer is characterized by low viscosity ( $10^{19}$  Pa s) and low density ( $1 \text{ kg m}^{-3}$ ).  
182 This boundary condition allows a relatively large integration time step and simulates surface  
183 faulting. The boundary condition at the bottom is free-slip. Material flows at 2 cm/year rate  
184 from the right-hand (east) side boundary and out at the left-hand side boundary beneath the  
185 orogenic lithosphere to maintain mass balance. The amount of shortening in our models (100

186 km) is appropriate and reasonable for shortening of the Central Andes over the last 10 Myr  
187 (Oncken et al., 2006; Horton, 2018). A higher but reasonable amount of shortening does not  
188 change the main results much (see **Figure S1** in the supporting information).

### 189 **3 Model Results**

#### 190 **3.1 Reference Model**

191 In reference Model M1, the orogen has the same lithospheric structure as the foreland  
192 except for the presence of a 4-km-thick sedimentary layer above the foreland. After 100 km  
193 shortening, the felsic crust undergoes pure-shear shortening, resulting in distributed crustal  
194 thickening and surface uplift (**Figure 2b**). **Figure 2c** shows that the strain rate norm (square  
195 root of the second invariant of the deviatoric strain rate) is homogeneously distributed from  
196 the surface to the basement at ~17 km depth. Thus, a fully thick-skinned tectonic style is  
197 formed in the foreland.

198 We conducted a series of modeling experiments to systematically investigate how the  
199 foreland deformation pattern is affected by changes in the lithospheric structure, crustal  
200 structure, and foreland sedimentary strength (**Table 2**; **Figure S2** in the supporting  
201 information). Below, we examine the effects of each of the following factors on the  
202 deformation style: (i) thickness of the orogenic lithosphere ( $H_{ol}$ ); (ii) thickness of the  
203 orogenic crust ( $H_{oc}$ ); (iii) thickness of the foreland lithosphere ( $H_{fl}$ ); (iv) friction  
204 coefficient of foreland sediments ( $\mu_{se}$ ); (v) thickness of foreland sediments ( $H_{se}$ ); and (vi)  
205 their combinations.

#### 206 **3.2 Variations in Orogenic and Foreland Lithospheric Structures**

##### 207 **3.2.1 Orogenic Lithospheric Thickness and Orogenic Crustal Thickness**

208 First, we intended to investigate the effect of orogenic lithospheric thickness on the  
209 foreland deformation pattern. Geological and geophysical observations indicate that the  
210 lithosphere under some active orogens (e.g., the Central Andes) is thin or absent (e.g., Beck &  
211 Zandt, 2002; Yuan et al., 2002). This is because the lithospheric mantle, being gravitationally  
212 unstable, is susceptible to partial removal via Rayleigh-Taylor-type instability (Molnar &  
213 Houseman, 2004) or complete removal by delamination (e.g., Bird, 1979; Le Pourhiet et al.,  
214 2006). In Model M2 (**Figure 3a**), the orogen has a 60-km-thick lithosphere and is weaker  
215 than the foreland in which the lithosphere is 100 km thick. The model result shows that the  
216 compressional deformation is localized within the orogen after 100 km pure-shear shortening.  
217 Simultaneously, a fully thick-skinned structure is formed in the foreland. In contrast, when the

218 initial lithosphere of the orogen is thicker and therefore stronger than that of the foreland (as  
219 in Model M3 in **Table 2**), the foreland deformation pattern remains unchanged. Therefore, in  
220 the models where only the orogenic lithospheric thickness changes while the crustal  
221 thicknesses in the orogen and its foreland remain the same, shortening of the foreland crust is  
222 in pure-shear mode accompanied by a fully thick-skinned tectonic style.

223         When the initial crust of the orogen thickens to 60 km, the foreland crust underthrusts  
224 beneath the orogen regardless of the thickness of the orogenic lithosphere within the range of  
225 parameters considered (**Table 2**), which is interpreted as a simple-shear shortening mode. In  
226 this mode, if the contribution of the thin-skinned deformation to the total foreland crustal  
227 deformation is less than one-tenth, then we consider this tectonic style to be thick-skinned  
228 dominated (e.g., M4-M6). The amount of simple-shear deformation appears to be greater in  
229 Model M4 (**Figure 3b**). It has a thinner orogenic lithosphere than in Model M6 (**Figure 3c**).  
230 In both models, a pronounced deep shear zone is produced between the upper and lower crust  
231 in the foreland.

### 232 **3.2.2 Foreland Lithospheric Thickness**

233         Here, we tested the effect of the foreland lithospheric strength on the deformation style  
234 by changing the foreland lithospheric thickness. In contrast, the initial crustal thicknesses in  
235 the foreland and the orogen were fixed. Unlike in the mountain belts, the foreland lithosphere  
236 in the craton can be thicker than 150 km. For example, the thermal lithosphere is >180 km  
237 thick under some foreland regions of southwestern Canadian craton (Currie, 2016). In Model  
238 M8 with a 200-km-thick foreland cratonic lithosphere, most of the shortening is concentrated  
239 in the orogenic crust, resulting in crustal buckling and surface uplift (**Figure 3d**). A fully  
240 thick-skinned structure is formed near the orogen-foreland boundary. As expected, the  
241 amount of foreland deformation decreases with the thickening of the foreland lithosphere  
242 (e.g., comparing M1 and M8).

### 243 **3.2.3 Foreland Sedimentary Strength**

244         The foreland sedimentary strength (coefficient of friction and its thickness) is also  
245 important for the foreland deformation pattern. Here, we varied the friction coefficient values  
246 of foreland sediments in the range of 0.58-0.02 (M1, M9-M10). This range is consistent with  
247 that of previous geodynamic models (e.g., Sobolev et al., 2006). The foreland deformation in  
248 Model M9 is no longer homogenous as in the reference model; pronounced thrust faults are  
249 produced in the middle part of the foreland (**Figure 3e**). When the friction coefficient of  
250 sediment is further reduced, and its thickness increases (M10), the magnitude of deformation

251 in the foreland increases, and the fault system becomes more complicated. However, the  
252 deformation pattern retains pure-shear shortening and fully thick-skinned tectonics. Regarding  
253 the factor of the thickness of foreland sediments, our model results show that the deformation  
254 pattern does not change if only the sedimentary thickness is increased, but less and deeper  
255 faulting occurs in the foreland crust (**Figure S2c**).

### 256 **3.2.4 Effects of Multiple Factors**

257 None of the above models shows a wide thin-skinned thrust zone in the foreland.  
258 Here, we present models combining multiple factors considered above (**Figure 3f-j**). All of  
259 these models have a 4-km-thick sedimentary layer in the foreland with a friction coefficient of  
260 0.05 (we term “weak foreland sedimentary layer”, i.e., the red area in the lithospheric  
261 structure bar in **Figure 3**). As we will see later, weak foreland sediments result in two  
262 additional tectonic styles thin- and thick-skinned mixed and fully thin-skinned. We deem the  
263 tectonic style to be mixed if its thin-skinned thrust zone is significantly wider than the zone in  
264 thick-skinned dominated tectonics (e.g., **Figure 3i**).

265 Weakening of foreland sediments in most models facilitates the underthrusting of the  
266 foreland beneath the orogen and promotes the formation of thin- and thick-skinned mixed or  
267 fully thin-skinned tectonics. The formation of the latter further requires a relatively thicker  
268 crust and/or thin lithosphere in the orogen (M12, M14, M17, M20). Foreland weak sediments  
269 can also switch the shortening mode from pure-shear to simple-shear (**Figure 3a, f**) when the  
270 crust in the orogen is thin but its lithosphere is thinner than the foreland lithosphere. This  
271 switch does not occur if the orogenic lithosphere is thicker (e.g., compare M3 and M7 with  
272 M13 and M15) or if the thicker foreland is in the cratonic area (**Figure 3d, h**). Additionally,  
273 these combined models show that large foreland underthrusting and mid-crustal viscous flow  
274 lead to crustal thickening and surface uplift in the orogen (**Figure 3g, j**).

## 275 **4 Discussion**

### 276 **4.1 Lithospheric Strength Analysis**

277 We calculated the initial integrated lithospheric strength of the orogen and its foreland  
278 and the strength ratio between them. The integrated strength is estimated through the  
279 integration of the yield strength envelope (e.g., Tesauro et al., 2013; Burov, 2011). Since the  
280 strength of the relatively thin sedimentary layer has little effect on the lithospheric strength,  
281 we neglected the strength change caused by the weakening of foreland sediments during the  
282 calculation. More details about the calculation are presented in the **Appendix**.

283 As we show below, foreland deformation styles are first-order controlled by the  
284 difference in lithospheric strength between the orogen and the foreland (**Figure 4**). We note,  
285 however, that the difference in the integrated strength of the entire lithosphere between the  
286 orogen and the foreland does not explain all model results. For example, the entire  
287 lithospheric strength of the orogen in Model M18, including a 150-km-thick lithosphere and a  
288 60-km-thick crust, is higher than that in Model M21 with an 80-km-thick lithosphere and a  
289 36-km-thick crust in the orogen (**Figure A1, S1**). Model M18 behaves in simple-shear  
290 shortening with thin- and thick-skinned mixed structures in the foreland (**Figure 3i**). As  
291 expected, if the model has a thinner and thus weaker orogenic lithosphere, it shows further  
292 underthrusting of the foreland beneath the orogen and a larger amount of thin-skinned  
293 deformation in the foreland (e.g., compare M14 with M18). However, the model behavior of  
294 M21 contradicts this view, where the tectonic type is thick-skinned dominated with a narrow  
295 thin-skinned wedge zone on the edge of the foreland (**Figure S2e**).

296 Therefore, we considered the strength difference of the upper part of the lithosphere  
297 between the orogen and its foreland, which controls the foreland deformation pattern better  
298 than the strength difference of the entire lithosphere (**Figure 4**). With this new definition of  
299 the upper lithospheric strength, Model M21 has a stronger upper orogenic lithosphere than  
300 Model M18, and therefore its strength ratio is higher. As a result, M21 shows less thin-  
301 skinned deformation in the foreland.

302 If the upper lithospheric strength in the orogen and its foreland are similar (strength  
303 ratio ~0.8-1.3 in **Figure 4**), the foreland (and the orogen) should deform in a pure-shear  
304 shortening mode accompanied by thick-skinned deformation. Less obvious is the foreland  
305 simple-shear mode and thin-skinned tectonics at a low strength ratio, i.e., when the orogenic  
306 lithosphere is much weaker than the foreland lithosphere. In this case, the intuitive scenario is  
307 the localization of shortening in the weak orogen rather than the foreland. However, the  
308 strong foreland in our models behaves in different deformation patterns. We infer that in  
309 addition to the lithospheric strength mentioned above, the gravitational potential energy  
310 (GPE) of the orogen also contributes to the foreland deformation pattern.

311 Generally, the compressive force driving orogenic shortening (i.e., mountain building)  
312 causes thickening of the orogenic crust. During shortening, the force works against two main  
313 resistive forces: the mechanical strength (discussed in this study) and gravity (e.g., Molnar &  
314 Lyon-Caen, 1988). The work against gravity creates the gravitational potential energy. The  
315 GPE per unit surface of the Earth area in the orogen increases with crustal thickening. Thus,  
316 shortening the orogen further requires an increasingly larger amount of work from the driving

317 force to overcome the increasing GPE. When the force can no longer supply the energy  
318 needed to elevate the orogen higher, the mountain range is likely to grow laterally in width  
319 instead of increasing in height and crustal thickness (Molnar & Lyon-Caen, 1988).  
320 Consequently, when the orogen grows laterally, the work done by the specified driving force  
321 will be used to deform the orogenic edge and its foreland, even if the orogenic lithosphere is  
322 much weaker than the foreland lithosphere. In this scenario, the foreland lithosphere can  
323 underthrust beneath the edge of the orogen, i.e., the foreland shortening mode is simple-shear  
324 (**Figure 4**). If there is a thick layer of mechanically weak sediments in the foreland, shear  
325 deformation is localized in the sedimentary layer and the foreland tectonic style is thin-  
326 skinned (**Figure 4b, d**). In this study, we treat the role of GPE as a reasonable qualitative  
327 assumption without testing its effect on lithospheric strength because the GPE of the orogen is  
328 in turn controlled by its crustal thickness and lithospheric thickness.

#### 329 **4.2 Structural Controls on the Shortening Mode and Tectonic Style in the Foreland**

330 Our model results demonstrate that the variation in orogenic strength caused by the  
331 change in orogenic crustal thickness has a critical effect on controlling the shortening mode.  
332 The pure-shear mode develops in the models with little difference in the crustal thickness  
333 between the orogen and the foreland, while the thickened orogenic crust is required to switch  
334 from pure-shear to simple-shear (**Figure 4**). The thickened orogenic crust causes the initially  
335 high GPE of the orogen and low strength of the orogenic upper lithosphere. This high GPE  
336 forces the shortening shift to the foreland. The thick and weak orogenic crust allows the  
337 strong foreland lithosphere to intrude into it in simple-shear mode easily. Our models show  
338 that the other four individual factors ( $H_{ol}$ ,  $H_{fl}$ ,  $\mu_{sed}$  and  $H_{sed}$ ) have little effect on the  
339 transition of the shortening mode with one exception. That is the case (the dashed rectangle in  
340 **Figure S2b**) when the orogenic crust is much thicker (high GPE) than the foreland crust and  
341 the foreland lithosphere is thin, showing a pure-shear shortening mode in the foreland.

342 Our models show that the significantly lower strength of the upper lithosphere in the  
343 orogen than in the foreland (strength ratio  $< \sim 0.7$ ) and the presence of thick and weak foreland  
344 sediments are responsible for the thin-skinned tectonics in the foreland. The absence of these  
345 conditions results in the tectonic style of fully thick-skinned or thick-skinned dominated.  
346 Furthermore, the condition of thick and weak foreland sediments generally intensifies simple-  
347 shear shortening by making underthrusting easier and thus broadening the thin-skinned thrust  
348 zone. When the orogenic crust is thick and the foreland lithosphere is thin, this condition can  
349 switch the shortening mode in the foreland from pure-shear to simple-shear.

### 350 **4.3 Applications to Natural Orogen-Foreland Shortening Systems**

351 Here, we compare our model inferences to the Central and Southern Andes and the  
352 Laramide orogeny and provide a first-order fit of the foreland deformation pattern to these  
353 natural shortening systems. We will look more specifically at the Altiplano-Puna plateau-  
354 foreland profile (**Figure 5b-c**), the Frontal Cordillera-Precordillera-Sierras Pampeanas profile  
355 (**Figure 5d**), and a more conceptual cross-section through the Colorado Plateau and Southern  
356 Rocky Mountain foreland (**Figure 5e-f**).

#### 357 **4.3.1 Altiplano-Puna Plateau**

358 In the Central Andes, the Altiplano-Puna Plateau was formed with N-S oriented  
359 deformation diversity, including a broad wedge-shaped thin-skinned thrust belt in the  
360 Interandean-Subandean zone and a thick-skinned structure in the Santa Barbara System  
361 (**Figure 5a**). The lithosphere under the plateau is very thin, but the upper felsic crust is as  
362 thick as 50-70 km (e.g., Tassara et al., 2006; Ibarra et al., 2019). This inherited thin  
363 lithosphere is suggested to result from lithospheric delamination, which occurred during  
364 Cenozoic shortening (e.g., Kay & Kay, 1993; Beck & Zandt, 2002; Sobolev & Babeyko,  
365 2005; Kay & Coira, 2009). The Puna Plateau and its foreland area have a higher seismic  
366 attenuation, implying a hotter and thinner lithosphere than the northern Altiplano part  
367 (Whitman et al., 1996). Paleozoic and Mesozoic sediments were abundantly deposited in the  
368 Subandean zone but pinched out southward to the Santa Barbara system (e.g., Allmendinger  
369 & Gubbels, 1996; Pearson et al., 2013). The local wet conditions in the foreland since the late  
370 Cenozoic (Strecker et al., 2007) indicate that abundant fluids are stored in these ancient  
371 sediments and may weaken them by increasing their pore fluid pressure.

372 We applied these observations to the model of the Central Andes. In the models  
373 (**Figure 5b-c**), the thickness of the orogenic crust under the Altiplano-Puna Plateau is 60 km.  
374 An additional 10-km-thick lithospheric mantle is attached to the Altiplano crust. The orogenic  
375 lithosphere under the Puna Plateau only contains thick crust due to mantle lithospheric  
376 delamination. The lithosphere of the Puna foreland in the model is 70 km thick and 30 km  
377 thinner than the Altiplano foreland lithosphere. In agreement with observations, the weak  
378 sedimentary layer in the model covers only the north Altiplano foreland crust (**Figure 5b**).  
379 Model results clearly show that the simple-shear mode with a fully thin-skinned thrust belt  
380 and the pure-shear mode with a fully thick-skinned structure are formed in the Altiplano  
381 foreland and the Puna foreland, respectively. Our models support and specify the results of  
382 previous relatively low-resolution modeling studies (e.g., Babeyko & Sobolev, 2005) and  
383 reproduce observed east-dipping reverse faults in the foreland edge in both cases.

### 384 4.3.2 Precordillera-Sierras Pampeanas Region

385 The Sierras Pampeanas province, located on the eastern side of the Precordillera thin-  
386 skinned thrust belts, is a modern analog of the thick-skinned deformation of the Laramide  
387 province (Jordan & Allmendinger, 1986). The tectonic style of the Precordillera-Sierras  
388 Pampeanas foreland region, adjacent to the Frontal Cordillera, can be broadly considered a  
389 thin- and thick-skinned mixed structure (**Figure 5a**). The oceanic flat slab below the Frontal  
390 Cordillera stays at 100 km depth, and thus, the orogenic lithosphere of the Frontal Cordillera  
391 may be less than 100 km thick (e.g., Jordan et al., 1983; Ramos & Folguera, 2009). The  
392 lithospheric thickness increases eastward and is more than 20 km thicker in the Sierras  
393 Pampeanas foreland. Crustal thickness exceeds 60 km beneath the Frontal Cordillera and  
394 rapidly decreases eastward to less than 40 km below its foreland (e.g., Ramos et al., 2004;  
395 Perarnau et al., 2012). Furthermore, there are abundant Paleozoic sedimentary rocks in the  
396 Precordillera, whereas only a small amount of Cenozoic sediments covers the Sierras  
397 Pampeanas (e.g., Ramos et al., 2004; Meeßen et al., 2018).

398 Unlike the 30°-dipping subducted slab in the Central Andean case, the southern  
399 Argentine Andean case slab is nearly horizontal (Jordan et al., 1983; Gutscher et al., 2000).  
400 Slab flattening can enhance the stress transmission from the subducting plate into the  
401 overlying plate by increasing the degree of plate coupling (e.g., Lacombe & Bellahsen, 2016),  
402 thus promoting plateau-foreland shortening, which may contribute to the development of  
403 thick-skinned tectonics. Note, however, that in the cases of the Sierras Pampeanas and the  
404 Laramide below, we do not introduce the factor of flat-slab subduction; therefore, our models  
405 do not exactly reproduce the amount of shortening and high topography of these two  
406 provinces.

407 The model constrained by these observations includes a thin and weak orogenic  
408 lithosphere 30 km thinner than the foreland lithosphere. Crustal thickness is greater than 60  
409 km in the orogen and decreases to ~ 40 km in the foreland. The model result (**Figure 5d**)  
410 indicates that simple-shear shortening occurs in the foreland, accompanied by mixed tectonics  
411 consisting of thin-skinned thrust at the foreland edge (Precordillera) and thick-skinned  
412 structure behind (Sierras Pampeanas). Note that the weak sedimentary layer is located through  
413 the entire foreland area in our model. Although it has little influence on the tectonic style of  
414 the Sierras Pampeanas, it is necessary to consider the difference in sedimentary thickness  
415 between the Precordillera and Sierras Pampeanas in future studies.

### 416 4.3.3 Laramide Province

417           The Laramide province (i.e., the Rocky Mountain foreland adjacent to the Colorado  
418 Plateau) is a widely thick-skinned deformation zone that developed more than 1000 km  
419 inboard the plate margin (e.g., Bird, 1984; Saleeby 2003; Erslev, 2013; Yonkee & Weil, 2015;  
420 Lacombe & Bellahsen, 2016). This province sustained more than 100 km pure-shear  
421 shortening, which contrasts strongly with minor deformation of the Colorado Plateau (e.g.,  
422 Bird, 1984; Spencer 1996; Flowers et al., 2008; Humphreys, 2009). Dynamic processes that  
423 propagate deformation across the strong and broad plateau far into the foreland and produce  
424 thick-skinned tectonics in the case of the Laramide orogeny are still largely debated.

425           One fashionable possibility is that the formation of the Laramide province is suggested  
426 to be the result of slab flattening of the Farallon plate. In particular, this process enhanced  
427 interplate coupling along the base of the cratonic lithosphere root, hence efficient stress  
428 transmission from the Farallon plate into the North American plate to deform the plateau-  
429 foreland system (e.g., Bird 1984; Axen et al., 2018). Furthermore, flat-slab subduction likely  
430 changed the strength of the continental lithospheric mantle. For instance, a cold slab can cool  
431 the above basal lithospheric mantle, which favors increased strength and stress transfer far  
432 into the foreland. In contrast, the lithospheric mantle can also be weakened due to the effects  
433 of basal lithospheric mantle removal by flat-slab subduction (e.g., Bird, 1984; Liu & Currie,  
434 2016; Axen et al., 2018), hydration from dewatering of the underlying flat slab and heating by  
435 magmatic ascent (Humphreys et al., 2003), and/or thermal inheritance from the preorogenic  
436 extension (Marshak et al., 2000). Lithospheric mantle weakening may allow shortening to  
437 occur in the deep mantle beneath the southern Rocky Mountains. Together with enhanced  
438 stress transfer, this process possibly promotes crustal shortening and leads to thick-skinned  
439 deformation within the foreland.

440           In addition to flat slab subduction, crustal/lithospheric buckling has been considered  
441 another possible mechanism for propagating and accommodating deformation in the  
442 Laramide foreland (e.g., Erslev, 1993; Tikoff & Maxson, 2001; Lacombe and Bellahsen, 2016  
443 and reference therein). For instance, Lacombe and Bellahsen (2016) emphasize that thick-  
444 skinned tectonics in the orogenic foreland is favored by the occurrence of a ductile middle or  
445 lower crust of a young, and hot lithosphere, hence enabling crust-mantle decoupling.  
446 Depending on its composition - felsic or mafic granulites - the middle or lower crust may  
447 have been either moderately weak with potential concentration of ductile flow along deep  
448 décollements or strong with potential for lithospheric buckling (Yonkee & Weil, 2015).  
449 Overall, intervening in specific boundary conditions such as flat slab subduction, together  
450 with structural crustal inheritance and possible mantle weakening, may provide a  
451 sophisticated explanation for intraplate basement-involved shortening in the Laramide setting.

452 As the deformation did not regularly propagate in a classical ‘in sequence’, foreland-  
453 ward way from the former Sevier orogen to the Laramide orogen, individual basement-cored  
454 deformation zones in the Laramide province may have developed spatially and temporally in  
455 a rather complex sequence (e.g., Crowley et al., 2002; Lacombe & Bellahsen, 2016). Since we  
456 are concentrated with the foreland deformation pattern during the Laramide orogeny, we  
457 simply developed a conceptual plateau-foreland shortening model constrained by  
458 observations of SW-NE tectonic transect through the Colorado Plateau and Southern Rocky  
459 Mountain foreland. This does not include the Sevier orogeny (**Figure 5e**). Although both  
460 western Farallon flat slab subduction and eastern intraplate shortening between the Colorado  
461 Plateau and the Rocky Mountain foreland can occur during Laramide deformation, we focus  
462 on the latter event. The subduction process is not integrated into the Laramide shortening  
463 model. Alternatively, we suppose that the presumptive flat-slab subduction on the left  
464 boundary prevents the leftward motion of the plateau. Hence, we close the left boundary  
465 above the orogenic lithosphere, resulting in a high degree of coupling between the plateau and  
466 its foreland.

467 In this transect, the Colorado Plateau and nearby Rocky Mountain foreland  
468 presumably involved a cool and thick lithosphere during the Laramide orogeny. Xenolith-  
469 based observations estimate the lithospheric thickness of the Colorado Plateau to be more  
470 than 150 km due to its underlying cold, refractory mantle root (e.g., Smith & Griffin, 2005; Li  
471 et al., 2008). Previous numerical studies of the flat slab subduction suggest that the Colorado  
472 Plateau may be thicker and thus stronger than its foreland cratonic lithosphere due to its deep  
473 cratonic root (e.g., O’Driscoll et al., 2009; Liu & Currie, 2016). The foreland was formerly  
474 part of a continental platform with an approximately 33-km-thick crust before the Laramide  
475 orogeny (Bird, 1984). The lower crust is cool, viscous, and largely intact beneath the  
476 Colorado Plateau (Humphreys et al., 2003). Lithostratigraphic columns of Laramide  
477 sedimentary successions in depocenters of key Laramide basins show that the thickness of the  
478 sedimentary cover is ~ 1-2 km (Dickinson et al., 1988).

479 To develop the model, we used a similar setup to the previous geodynamic models of  
480 the Laramide (Liu & Currie, 2016) and further constrained it with the above observations. In  
481 this model, the plateau lithosphere is 240 km thick, 40 km thicker than the foreland  
482 lithosphere. The foreland crust is 10 km thinner than the orogenic crust and includes a 2-km-  
483 thick sedimentary layer. When the strength of the upper lithosphere of the orogen is slightly  
484 greater than that of the foreland (the hollow star of the Laramide-R.M. case in **Figure 4c**), the  
485 foreland is subjected to pure-shear shortening with fully thick-skinned tectonics (**Figure 3f**),

486 and there is minor deformation in the plateau. Foreland deformation is mainly accommodated  
487 in the felsic upper-middle crust, potentially implying decoupling between the felsic upper-  
488 middle crust and mafic lower crust and lithospheric mantle. Our model results support the  
489 mechanism of lithospheric buckling in Laramide deformation.

490 Note that we have not attempted to provide a thorough review of the  
491 Andean/Laramide orogeny. Rather, we have attempted to demonstrate that the foreland  
492 deformation pattern of the Andean/Laramide orogeny is consistent with simplified orogen-  
493 foreland shortening models. The very fine internal structure of the deformed sediments is not  
494 visible in our models and is modeled as a zone with a finite strain greater than 1. This is  
495 because our models did not employ a deformed mesh used in Erdős et al. (2015) and Jammes  
496 and Huismans (2012), although the resolution of our models is sufficient. We have addressed  
497 only the contrast in the lithospheric strength between the orogen and foreland and the strength  
498 of the foreland sediment within these shortening models. Other parameters (e.g., the rate and  
499 amount of shortening, subduction dynamics, and thermal/structural inheritance) have not been  
500 addressed here but are necessary to be considered in future comprehensive case studies.

## 501 **5 Conclusions**

502 With high-resolution thermomechanical numerical models, we systematically examine  
503 the effects of the lithospheric structure and foreland sedimentary strength on the foreland  
504 deformation pattern subjected to tectonic shortening.

505 We find that three factors significantly control the shortening mode (pure-shear or  
506 simple-shear) and the tectonic style (thick-skinned or thin-skinned): (i) the strength difference  
507 in the upper lithosphere between the orogen and its foreland, rather than the difference in the  
508 entire lithospheric strength between them; (ii) GPE of the orogen that is in turn controlled by  
509 its crustal thickness and lithospheric thickness; and (iii) the strength and thickness of the  
510 deforming foreland sediments.

511 If the strength of the orogenic upper lithosphere is higher or similar to that of the  
512 foreland upper lithosphere (strength ratio  $> \sim 0.8$ ) and the orogenic crust is not much thicker  
513 than the foreland crust (relatively low GPE of the orogen), pure-shear shortening develops in  
514 the foreland.

515 If the strength of the orogenic upper lithosphere is significantly lower than that of the  
516 foreland upper lithosphere (strength ratio  $< \sim 0.7$ ) and the orogenic crust is much thicker than  
517 the foreland crust ( $> 50$  km causing relatively high GPE of the orogen), the foreland  
518 undergoes simple-shear shortening.

519 In the particular case of thick orogenic crust (> 50 km, high GPE) and thin (< 70 km)  
520 orogenic lithosphere and simultaneously thin (< 70-80 km) foreland lithosphere, the foreland  
521 shortening mode is pure-shear (Puna-Santa Barbara system case).

522 Fully thin-skinned or thin- and thick-skinned mixed tectonic styles can develop in the  
523 foreland only if thick (> ~4 km) and mechanically weak (friction coefficient < ~0.05)  
524 sediments are present in the simple-shear shortening mode. Furthermore, the most  
525 pronounced fully thin-skinned tectonics develops in the thick and weak foreland sedimentary  
526 layer when the strength of the orogenic upper lithosphere is much lower than that of the  
527 foreland upper lithosphere (strength ratio < 0.3-0.4; Altiplano-Subandean ranges case).

528 Our high-resolution orogen-foreland shortening models successfully reproduce  
529 foreland deformation patterns in the Central and Southern Andes in South America during the  
530 Neogene and Laramide province in North America during the Late Cretaceous to Paleocene.

### 531 **Acknowledgements**

532 The research is within the framework of the project *IGK 2018 SuRfAce processes,*  
533 *Tectonics and Georesources: The Andean foreland basin of Argentina (StRATEGy)* and  
534 funded by the Deutsche Forschungsgemeinschaft (DFG, grant STR 373/34-1) and the  
535 Brandenburg Ministry of Sciences, Research and Cultural Affairs, Germany. The open-source  
536 code LaMEM can be found at <https://bitbucket.org/bkaus/LaMEM>. For this paper we used the  
537 master branch and commit version b58966b. Computations were performed with resources  
538 provided by the North-German Supercomputing Alliance (HLRN). Input files used to produce  
539 the model results are available at [https://github.com/sibiaoliu/paper-Orogen-Foreland-](https://github.com/sibiaoliu/paper-Orogen-Foreland-Shortening-System)  
540 *Shortening-System*. We thank Olivier Lacombe and Laetitia Le Pourhiet for their thoughtful  
541 review comments, Peter van der Beek, Zoltán Erdős, and one anonymous reviewer for their  
542 comments on an earlier draft of this manuscript.

### 543 **Appendix: Geodynamic Governing Equations and Yield Strength Envelope**

544 Material deformation is governed by solving the coupled system of momentum (1),  
545 mass (2), and energy (3) conservation equations below:

$$546 \quad \frac{\partial \tau_{ij}}{\partial x_j} - \frac{\partial P}{\partial x_i} + \rho g_i = 0 \quad (1)$$

$$547 \quad \frac{\partial v_i}{\partial x_i} = 0 \quad (2)$$

$$548 \quad \rho C_p \frac{DT}{Dt} = \frac{\partial}{\partial x_i} \left( k \frac{\partial T}{\partial x_i} \right) + \tau_{ij} \left( \dot{\epsilon}_{ij}^v + \dot{\epsilon}_{ij}^p \right) + \rho A \quad (3)$$

549 where  $i, j$  represent spatial directions following Einstein summation convention,  $x_{ij}$  are  
 550 the Cartesian coordinates,  $\tau_{ij}$  is the deviatoric stress tensor,  $P$  is pressure,  $\rho$  is the density,  $g_i$  is  
 551 the gravitational acceleration vector,  $v_i$  and  $v_j$  are components of the velocity,  $D/Dt$  is the  
 552 material time derivative,  $C_p$  is specific heat,  $k$  is thermal conductivity,  $A$  is the radiogenic heat  
 553 production, and  $\dot{\epsilon}_{ij}^v, \dot{\epsilon}_{ij}^p$  are viscous and plastic strain-rate deviators, respectively. Repeated  
 554 indices imply summation. These basic geodynamic equations are solved assuming plane  
 555 strain, incompressibility, and neglecting thermal diffusion.

556 The material behaves the frictional-plastic deformation when the deviatoric stress  
 557 exceeds the plastic yield stress ( $\tau_Y$ ), which follows a pressure-dependent Drucker-Prager yield  
 558 criterion:

$$559 \quad \tau_Y = P \sin \varphi + C_0 \cos \varphi \quad (4)$$

560 where  $\varphi$  is the internal friction angle and  $C_0$  is the cohesion. We assume the friction  
 561 coefficient  $\mu = \tan(\varphi)$ . Below this yield stress, materials deform viscously with an effective  
 562 viscosity ( $\eta_{\text{eff}}$ ) given by:

$$563 \quad \eta_{\text{eff}} = \frac{1}{2B^{1/n}} \dot{\epsilon}_{II}^{(1-n)/n} \exp\left(\frac{E+PV}{nRT}\right) \quad (5)$$

564 where  $\dot{\epsilon}_{II} = \sqrt{\frac{1}{2} \dot{\epsilon}_{ij} \dot{\epsilon}_{ij}}$  is the second invariant of the square root of the deviatoric strain  
 565 rate,  $\dot{\epsilon}_{ij} = \frac{1}{2} \left( \frac{\partial v_i}{\partial x_j} + \frac{\partial v_j}{\partial x_i} \right)$ ,  $R$  is the gas constant.  $B, n, E, V$  are the laboratory-derived pre-  
 566 exponential viscosity parameter, stress exponent, activation energy and activation volume,  
 567 respectively.

568 Integrated strength of the lithosphere ( $\sigma_L$ ) under compression is estimated from the  
 569 yield strength envelope (YSE):

$$570 \quad \sigma_L = \int_0^h (\sigma_1 - \sigma_3) dz = \int_0^h \min(\sigma_B, \sigma_D) dz \quad (6)$$

571 where  $h$  is the lithospheric thickness,  $\sigma_1$  and  $\sigma_3$  are the maximum and minimum  
 572 principal stress component, respectively. **Figure A1** shows initial strength envelopes of the  
 573 lithosphere with different structures. There are two different types in the envelope: the  
 574 frictional brittle strength ( $\sigma_B$ ; the purple line in **Figure A1**) and the ductile strength ( $\sigma_D$ ;  
 575 dashed colored curves in **Figure A1**). The brittle strength is estimated by the Byerlee's law  
 576 (Byerlee, 1978) and a function of pressure-independent rock types in a compressional  
 577 environment:  $\sigma_B = \int_0^h 2\mu(\sqrt{\mu^2 + 1} + \mu)\rho g(1 - \lambda) dz$ . The pore fluid factor ( $\lambda$ ) is 0.36. The

578 ductile strength  $\sigma_D = \left(\frac{\dot{\epsilon}_{\text{ref}}}{B}\right)^{\frac{1}{n}} \exp\left(\frac{E+PV}{nRT}\right)$ . The initial reference strain rate ( $\dot{\epsilon}_{\text{ref}}$ ) is  $10^{-16} \text{ s}^{-1}$ . The  
579 viscous parameters are corresponding to the dislocation creep mechanism.

## 580 **References**

- 581 Allmendinger, R. W., & Gubbels, T. (1996). Pure and simple shear plateau uplift, Altiplano-  
582 Puna, Argentina and Bolivia. *Tectonophysics*, 259(1), 1–13.  
583 [https://doi.org/10.1016/0040-1951\(96\)00024-8](https://doi.org/10.1016/0040-1951(96)00024-8).
- 584 Axen, G. J., van Wijk, J. W., & Currie, C. A. (2018). Basal continental mantle lithosphere  
585 displaced by flat-slab subduction. *Nature Geoscience*, 11(12), 961–964.  
586 <https://doi.org/10.1038/s41561-018-0263-9>.
- 587 Babeyko, A. Y., & Sobolev, S. V. (2005). Quantifying different modes of the late Cenozoic  
588 shortening in the central Andes. *Geology*, 33(8), 621–624.  
589 <https://doi.org/10.1130/G21126AR.1>.
- 590 Babeyko, A. Y., Sobolev, S. V., Vietor, T., Oncken, O., & Trumbull, R. B. (2006). Numerical  
591 Study of Weakening Processes in the Central Andean Back-Arc. In O. Oncken, G.  
592 Chong, G. Franz, P. Giese, H.-J. Götze, V. A. Ramos, et al. (Eds.), *The Andes* (pp.  
593 495–512). Springer Berlin Heidelberg. Retrieved from  
594 [http://link.springer.com/10.1007/978-3-540-48684-8\\_24](http://link.springer.com/10.1007/978-3-540-48684-8_24).
- 595 Barrionuevo, M., Liu, S., Mescua, J., Yagupsky, D., Quinteros, J., Giambiagi, L., Sobolev, S.  
596 V., Picada, C. R., Strecker, M. R. (2021). The influence of variations in crustal  
597 composition and lithospheric strength on the evolution of deformation processes in the  
598 southern Central Andes: insights from geodynamic models. *International Journal of*  
599 *Earth Sciences*, 110(7), 2361–2384.
- 600 Beck, S. L., & Zandt, G. (2002). The nature of orogenic crust in the central Andes. *Journal of*  
601 *Geophysical Research: Solid Earth*, 107(B10), ESE 7-1-ESE 7-16.  
602 <https://doi.org/10.1029/2000JB000124>.
- 603 Bellahsen, N., Mouthereau, F., Boutoux, A., Bellanger, M., Lacombe, O., Jolivet, L., &  
604 Rolland, Y. (2014). Collision kinematics in the western external Alps. *Tectonics*,  
605 33(6), 1055–1088. <https://doi.org/10.1002/2013TC003453>.
- 606 Bellahsen, N., Sebrier, M., & Siame, L. (2016). Crustal shortening at the Sierra Pie de Palo  
607 (Sierras Pampeanas, Argentina): near-surface basement folding and thrusting.  
608 *Geological Magazine*, 153(5–6), 992–1012.  
609 <https://doi.org/10.1017/S0016756816000467>.

- 610 Bird, P. (1979). Continental delamination and the Colorado Plateau. *Journal of Geophysical*  
611 *Research: Solid Earth*, 84(B13), 7561–7571.  
612 <https://doi.org/10.1029/JB084iB13p07561>.
- 613 Bird, P. (1984). Laramide crustal thickening event in the Rocky Mountain Foreland and Great  
614 Plains. *Tectonics*, 3(7), 741–758. <https://doi.org/10.1029/TC003i007p00741>.
- 615 Burov, E. B., & Watts, A. B. (2006). The long-term strength of continental lithosphere: jelly-  
616 sandwich or crème-brûlée?. *GSA Today*, 16(1), 4-10. [https://doi.org/10.1130/1052-  
617 5173\(2006\)016<4:TLTSOC>2.0.CO;2](https://doi.org/10.1130/1052-5173(2006)016<4:TLTSOC>2.0.CO;2).
- 618 Burov, E. B. (2011). Rheology and strength of the lithosphere. *Marine and Petroleum*  
619 *Geology*, 28(8), 1402–1443. <https://doi.org/10.1016/j.marpetgeo.2011.05.008>.
- 620 Byerlee, J. (1978). Friction of rocks. *Pure and Applied Geophysics*, 116(4–5), 615–626.  
621 <https://doi.org/10.1007/BF00876528>.
- 622 Cloetingh, S., & Burov, E. B. (1996). Thermomechanical structure of European continental  
623 lithosphere: constraints from rheological profiles and EET estimates. *Geophysical*  
624 *Journal International*, 124(3), 695–723. [https://doi.org/10.1111/j.1365-  
625 246X.1996.tb05633.x](https://doi.org/10.1111/j.1365-246X.1996.tb05633.x).
- 626 Cobbold, P. R., Mourgues, R., & Boyd, K. (2004). Mechanism of thin-skinned detachment in  
627 the Amazon Fan: assessing the importance of fluid overpressure and hydrocarbon  
628 generation. *Marine and Petroleum Geology*, 21(8), 1013–1025.  
629 <https://doi.org/10.1016/j.marpetgeo.2004.05.003>.
- 630 Crowley, P. D., Reiners, P. W., Reuter, J. M., & Kaye, G. D. (2002). Laramide exhumation of  
631 the Bighorn Mountains, Wyoming: An apatite (U-Th)/He thermochronology study.  
632 *Geology*, 30(1), 27–30. [https://doi.org/10.1130/0091-  
633 7613\(2002\)030<0027:LEOTBM>2.0.CO;2](https://doi.org/10.1130/0091-7613(2002)030<0027:LEOTBM>2.0.CO;2).
- 634 Currie, C. A. (2016). The Deep Roots of the Rocky Mountains: Geophysical Studies of  
635 Western Canada. *Journal of Student Science and Technology*, 9(1).  
636 <https://doi.org/10.13034/jsst.v9i1.142>.
- 637 Dahlen, F. A. (1990). Critical Taper Model of Fold-And-Thrust Belts and Accretionary  
638 Wedges. *Annual Review of Earth and Planetary Sciences*, 18(1), 55–99.  
639 <https://doi.org/10.1146/annurev.ea.18.050190.000415>.
- 640 DeCelles, P. G. (2004). Late Jurassic to Eocene evolution of the Cordilleran thrust belt and  
641 foreland basin system, western U.S.A. *American Journal of Science*, 304(2), 105–168.  
642 <https://doi.org/10.2475/ajs.304.2.105>.
- 643 Dickinson, W., Klute, M., Hayes, M., Janecke, S., Lundin, E., McKittrick, M., & Olivares, M.  
644 (1988). Paleogeographic and paleotectonic setting of Laramide sedimentary basins in

645 the central Rocky Mountain region. *Geological Society of America Bulletin - GEOL*  
646 *SOC AMER BULL*, 100. <https://doi.org/10.1130/0016->  
647 7606(1988)100<1023:PAPSOL>2.3.CO;2.

648 Ellis, M. (1988). Lithospheric Strength in Compression: Initiation of Subduction, Flake  
649 Tectonics, Foreland Migration of Thrusting, and an Origin of Displaced Terranes. *The*  
650 *Journal of Geology*, 96(1), 91–100. <https://doi.org/10.1086/629195>.

651 Erdős, Z., Huisman, R. S., & van der Beek, P. (2015). First-order control of syntectonic  
652 sedimentation on crustal-scale structure of mountain belts. *Journal of Geophysical*  
653 *Research: Solid Earth*, 120(7), 5362–5377. <https://doi.org/10.1002/2014JB011785>.

654 Erslev, E. A. (2013). 2D Laramide Geometries and Kinematics of the Rocky Mountains,  
655 Western U.S.A. In *The Rocky Mountain Region: An Evolving Lithosphere* (pp. 7–20).  
656 American Geophysical Union (AGU). <https://doi.org/10.1029/154GM02>.

657 Flowers, R. M., Wernicke, B., & Farley, K. (2008). Unroofing, incision, and uplift history of  
658 the southwestern Colorado Plateau from apatite (U-Th)/He thermochronometry.  
659 *Geological Society of America Bulletin*, 120. <https://doi.org/10.1130/B26231.1>.

660 Giambiagi, L., Mescua, J., Bechis, F., Martínez, A., & Folguera, A. (2011). Pre-Andean  
661 deformation of the Precordillera southern sector, southern Central Andes. *Geosphere*,  
662 7(1), 219–239. <https://doi.org/10.1130/GES00572.1>.

663 Gleason, G. C., & Tullis, J. (1995). A flow law for dislocation creep of quartz aggregates  
664 determined with the molten salt cell. *Tectonophysics*, 247(1), 1–23.  
665 [https://doi.org/10.1016/0040-1951\(95\)00011-B](https://doi.org/10.1016/0040-1951(95)00011-B).

666 Hassani, R., Jongmans, D., & Chéry, J. (1997). Study of plate deformation and stress in  
667 subduction processes using two-dimensional numerical models. *Journal of*  
668 *Geophysical Research: Solid Earth*, 102(B8), 17951–17965.  
669 <https://doi.org/10.1029/97JB01354>.

670 Hirth, G., & Kohlstedt, D. (2003). Rheology of the upper mantle and the mantle wedge: A  
671 view from the experimentalists. *Washington DC American Geophysical Union*  
672 *Geophysical Monograph Series*, 138, 83–105. <https://doi.org/10.1029/138GM06>.

673 Holt, W. E., & Wallace, T. C. (1990). Crustal thickness and upper mantle velocities in the  
674 Tibetan Plateau Region from the inversion of regional Pnl waveforms: Evidence for a  
675 thick upper mantle lid beneath southern Tibet. *Journal of Geophysical Research: Solid*  
676 *Earth*, 95(B8), 12499–12525. <https://doi.org/10.1029/JB095iB08p12499>.

677 Humphreys, E. (2009). Relation of flat subduction to magmatism and deformation in the  
678 western United States. *Geological Society of America Memoirs*, 204(0), 85–98.  
679 [https://doi.org/10.1130/2009.1204\(04\)](https://doi.org/10.1130/2009.1204(04)).

680 Humphreys, E., Hessler, E., Dueker, K., Farmer, G. L., Erslev, E., & Atwater, T. (2003). How  
681 Laramide-Age Hydration of North American Lithosphere by the Farallon Slab  
682 Controlled Subsequent Activity in the Western United States. *International Geology*  
683 *Review*, 45(7), 575–595. <https://doi.org/10.2747/0020-6814.45.7.575>.

684 Ibarra, F., Liu, S., Meeßen, C., Prezzi, C. B., Bott, J., Scheck-Wenderoth, M., et al. (2019).  
685 3D data-derived lithospheric structure of the Central Andes and its implications for  
686 deformation: Insights from gravity and geodynamic modelling. *Tectonophysics*, 766,  
687 453–468. <https://doi.org/10.1016/j.tecto.2019.06.025>.

688 Jammes, S., & Huisman, R. S. (2012). Structural styles of mountain building: Controls of  
689 lithospheric rheologic stratification and extensional inheritance. *Journal of*  
690 *Geophysical Research: Solid Earth*, 117(B10). <https://doi.org/10.1029/2012JB009376>.

691 Jordan, T. E., & Allmendinger, R. W. (1986). The Sierras Pampeanas of Argentina; a modern  
692 analogue of Rocky Mountain foreland deformation. *American Journal of Science*,  
693 286(10), 737–764. <https://doi.org/10.2475/ajs.286.10.737>.

694 Jordan, T. E., Isacks, B. L., Allmendinger, R. W., Brewer, J. A., Ramos, V. A., & Ando, C. J.  
695 (1983). Andean tectonics related to geometry of subducted Nazca plate. *GSA Bulletin*,  
696 94(3), 341–361. [https://doi.org/10.1130/0016-](https://doi.org/10.1130/0016-7606(1983)94<341:ATRTGO>2.0.CO;2)  
697 [7606\(1983\)94<341:ATRTGO>2.0.CO;2](https://doi.org/10.1130/0016-7606(1983)94<341:ATRTGO>2.0.CO;2).

698 Kaus, B. J. P., Mühlhaus, H., & May, D. A. (2010). A stabilization algorithm for geodynamic  
699 numerical simulations with a free surface. *Physics of the Earth and Planetary*  
700 *Interiors*, 181(1–2), 12–20. <https://doi.org/10.1016/j.pepi.2010.04.007>.

701 Kaus, B. J. P., Popov, A. A., Baumann, T. S., Pusok, A. E., Bauville, A., Fernandez, N., &  
702 Collignon, M. (2016). Forward and inverse modelling of lithospheric deformation on  
703 geological timescales. *NIC Symposium 2016 - Proceedings*, 48, 299–307.

704 Kay, R. W., & Kay, S. M. (1993). Delamination and delamination magmatism.  
705 *Tectonophysics*, 219(1), 177–189. [https://doi.org/10.1016/0040-1951\(93\)90295-U](https://doi.org/10.1016/0040-1951(93)90295-U).

706 Kay, S. M., & Coira, B. L. (2009). Shallowing and steepening subduction zones, continental  
707 lithospheric loss, magmatism, and crustal flow under the Central Andean Altiplano-  
708 Puna Plateau. *Geological Society of America Memoirs*, 204, 229–259.  
709 [https://doi.org/10.1130/2009.1204\(11\)](https://doi.org/10.1130/2009.1204(11)).

710 Kley, J., Monaldi, C. R., & Salfity, J. A. (1999). Along-strike segmentation of the Andean  
711 foreland: causes and consequences. *Tectonophysics*, 301(1–2), 75–94.  
712 [https://doi.org/10.1016/S0040-1951\(98\)90223-2](https://doi.org/10.1016/S0040-1951(98)90223-2).

- 713 Kohlstedt, D. L., Evans, B., & Mackwell, S. J. (1995). Strength of the lithosphere: Constraints  
714 imposed by laboratory experiments. *Journal of Geophysical Research: Solid Earth*,  
715 *100*(B9), 17587–17602. <https://doi.org/10.1029/95JB01460>.
- 716 Kuszniir, N. J., & Park, R. G. (1986). Continental lithosphere strength: the critical role of  
717 lower crustal deformation. *Geological Society, London, Special Publications*, *24*(1),  
718 79–93. <https://doi.org/10.1144/GSL.SP.1986.024.01.09>.
- 719 Lacombe, O., & Mouthereau, F. (2002). Basement-involved shortening and deep detachment  
720 tectonics in forelands of orogens: Insights from recent collision belts (Taiwan,  
721 Western Alps, Pyrenees). *Tectonics*, *21*(4), 12–1.  
722 <https://doi.org/10.1029/2001TC901018>.
- 723 Lacombe, O., & Bellahsen, N. (2016). Thick-skinned tectonics and basement-involved fold–  
724 thrust belts: insights from selected Cenozoic orogens. *Geological Magazine*, *153*(5–6),  
725 763–810. <https://doi.org/10.1017/S0016756816000078>.
- 726 Laske, G., Masters, T. G., Ma, Z., & Pasyanos, M. E. (2013). Update on CRUST1.0: A 1-  
727 degree Global Model of Earth’s Crust.
- 728 Le Pourhiet, L., Gurnis, M., & Saleeby, J. (2006). Mantle instability beneath the Sierra  
729 Nevada Mountains in California and Death Valley extension. *Earth and Planetary  
730 Science Letters*, *251*(1–2), 104–119. <https://doi.org/10.1016/j.epsl.2006.08.028>.
- 731 Li A. Z., Lee C. A., Peslier A. H., Lenardic A., & Mackwell S. J. (2008). Water contents in  
732 mantle xenoliths from the Colorado Plateau and vicinity: Implications for the mantle  
733 rheology and hydration-induced thinning of continental lithosphere. *Journal of  
734 Geophysical Research: Solid Earth*, *113*(B9). <https://doi.org/10.1029/2007JB005540>.
- 735 Liu, S., & Currie, C. A. (2016). Farallon plate dynamics prior to the Laramide orogeny:  
736 Numerical models of flat subduction. *Tectonophysics*, *666*, 33–47.  
737 <https://doi.org/10.1016/j.tecto.2015.10.010>.
- 738 Mackwell, S. J., Zimmerman, M. E., & Kohlstedt, D. L. (1998). High-temperature  
739 deformation of dry diabase with application to tectonics on Venus. *Journal of  
740 Geophysical Research: Solid Earth*, *103*(B1), 975–984.  
741 <https://doi.org/10.1029/97JB02671>.
- 742 Marshak, S., Karlstrom, K., & Timmons, J. M. (2000). Inversion of Proterozoic extensional  
743 faults: An explanation for the pattern of Laramide and Ancestral Rockies intracratonic  
744 deformation, United States. *Geology*, *28*(8), 735–738. [https://doi.org/10.1130/0091-  
745 7613\(2000\)28<735:IOPEFA>2.0.CO;2](https://doi.org/10.1130/0091-7613(2000)28<735:IOPEFA>2.0.CO;2).
- 746 Meeßen, C., Sippel, J., Scheck-Wenderoth, M., Heine, C., & Strecker, M. R. (2018). Crustal  
747 Structure of the Andean Foreland in Northern Argentina: Results From Data-

748 Integrative Three-Dimensional Density Modeling. *Journal of Geophysical Research:*  
749 *Solid Earth*. <https://doi.org/10.1002/2017JB014296>.

750 Mescua, J. F., Giambiagi, L., Barrionuevo, M., Tassara, A., Mardonez, D., Mazzitelli, M., &  
751 Lossada, A. (2016). Basement composition and basin geometry controls on upper-  
752 crustal deformation in the Southern Central Andes (30–36°S). *Geological Magazine*,  
753 *153*(5–6), 945–961. <https://doi.org/10.1017/S0016756816000364>.

754 Molnar, P., & Houseman, G. A. (2004). The effects of buoyant crust on the gravitational  
755 instability of thickened mantle lithosphere at zones of intracontinental convergence.  
756 *Geophysical Journal International*, *158*(3), 1134–1150.  
757 <https://doi.org/10.1111/j.1365-246X.2004.02312.x>.

758 Molnar, P., & Lyon-Caen, H. (1988). Some simple physical aspects of the support, structure,  
759 and evolution of mountain belts. In *Geological Society of America Special Papers*  
760 (Vol. 218, pp. 179–208). Geological Society of America.  
761 <https://doi.org/10.1130/SPE218-p179>.

762 Mouthereau, F., & Lacombe, O. (2006). Inversion of the Paleogene Chinese continental  
763 margin and thick-skinned deformation in the Western Foreland of Taiwan. *Journal of*  
764 *Structural Geology*, *28*(11), 1977–1993. <https://doi.org/10.1016/j.jsg.2006.08.007>.

765 Mouthereau, F., Lacombe, O., & Meyer, B. (2006). The Zagros folded belt (Fars, Iran):  
766 constraints from topography and critical wedge modelling. *Geophysical Journal*  
767 *International*, *165*(1), 336–356. <https://doi.org/10.1111/j.1365-246X.2006.02855.x>.

768 Mouthereau, F., Tensi, J., Bellahsen, N., Lacombe, O., De Boisgrollier, T., & Kargar, S.  
769 (2007). Tertiary sequence of deformation in a thin-skinned/thick-skinned collision  
770 belt: The Zagros Folded Belt (Fars, Iran). *Tectonics*, *26*(5).  
771 <https://doi.org/10.1029/2007TC002098>.

772 Mouthereau, F., Lacombe, O., & Vergés, J. (2012). Building the Zagros collisional orogen:  
773 Timing, strain distribution and the dynamics of Arabia/Eurasia plate convergence.  
774 *Tectonophysics*, *532–535*, 27–60. <https://doi.org/10.1016/j.tecto.2012.01.022>.

775 Nilfouroushan, F., Pysklywec, R., Cruden, A., & Koyi, H. (2013). Thermal-mechanical  
776 modeling of salt-based mountain belts with pre-existing basement faults: Application  
777 to the Zagros fold and thrust belt, southwest Iran. *Tectonics*, *32*(5), 1212–1226.  
778 <https://doi.org/10.1002/tect.20075>.

779 O’Driscoll, L. J., Humphreys, E. D., & Saucier, F. (2009). Subduction adjacent to deep  
780 continental roots: Enhanced negative pressure in the mantle wedge, mountain building  
781 and continental motion. *Earth and Planetary Science Letters*, *280*(1), 61–70.  
782 <https://doi.org/10.1016/j.epsl.2009.01.020>.

- 783 Oncken, O., Chong, G., Franz, G., Giese, P., Götze, H.-J., Ramos, V. A., et al. (2006). The  
784 Andes: Active Subduction Orogeny. Springer Science & Business Media.
- 785 Pearson, D. M., Kapp, P., DeCelles, P. G., Reiners, P. W., Gehrels, G. E., Ducea, M. N., &  
786 Pullen, A. (2013). Influence of pre-Andean crustal structure on Cenozoic thrust belt  
787 kinematics and shortening magnitude: Northwestern Argentina. *Geosphere*, 9(6),  
788 1766–1782. <https://doi.org/10.1130/GES00923.1>.
- 789 Perarnau, M., Gilbert, H., Alvarado, P., Martino, R., & Anderson, M. (2012). Crustal structure  
790 of the Eastern Sierras Pampeanas of Argentina using high frequency local receiver  
791 functions. *Tectonophysics*, 580, 208–217. <https://doi.org/10.1016/j.tecto.2012.09.021>.
- 792 Pfiffner, O. A. (2016). Basement-involved thin-skinned and thick-skinned tectonics in the  
793 Alps. *Geological Magazine*, 153(5–6), 1085–1109.  
794 <https://doi.org/10.1017/S0016756815001090>.
- 795 Pfiffner, O. A. (2017). Thick-Skinned and Thin-Skinned Tectonics: A Global Perspective.  
796 *Geosciences*, 7(3), 71. <https://doi.org/10.3390/geosciences7030071>.
- 797 Poudjom Djomani, Y. H., O'Reilly, S. Y., Griffin, W. L., & Morgan, P. (2001). The density  
798 structure of subcontinental lithosphere through time. *Earth and Planetary Science  
799 Letters*, 184(3), 605–621. [https://doi.org/10.1016/S0012-821X\(00\)00362-9](https://doi.org/10.1016/S0012-821X(00)00362-9).
- 800 Price, R. A. (1981). The Cordilleran foreland thrust and fold belt in the southern Canadian  
801 Rocky Mountains. *Geological Society, London, Special Publications*, 9(1), 427–448.  
802 <https://doi.org/10.1144/GSL.SP.1981.009.01.39>.
- 803 Ramos, V. A., & Folguera, A. (2009). Andean flat-slab subduction through time. *Geological  
804 Society, London, Special Publications*, 327(1), 31–54.  
805 <https://doi.org/10.1144/SP327.3>.
- 806 Ramos, V. A., Zapata, T., Cristallini, E., & Introcaso, A. (2004). The Andean Thrust System  
807 Latitudinal Variations in Structural Styles and Orogenic Shortening, 30–50.
- 808 Saleeby, J. (2003). Segmentation of the Laramide Slab—evidence from the southern Sierra  
809 Nevada region. *GSA Bulletin*, 115(6), 655–668. [https://doi.org/10.1130/0016-  
810 7606\(2003\)115<0655:SOTLSF>2.0.CO;2](https://doi.org/10.1130/0016-7606(2003)115<0655:SOTLSF>2.0.CO;2).
- 811 Siame, L., Bellier, O., & Sébrier, M. (2006). Active tectonics in the Argentine Precordillera  
812 and Western Sierras Pampeanas. *Revista de La Asociacion Geologica Argentina*, 61,  
813 604–619.
- 814 Smith, D., & Griffin, W. L. (2005). Garnetite Xenoliths and Mantle–Water Interactions  
815 Below the Colorado Plateau, Southwestern United States. *Journal of Petrology*, 46(9),  
816 1901–1924. <https://doi.org/10.1093/petrology/egi042>.

- 817 Sobolev, S. V., & Babeyko, A. Y. (2005). What drives orogeny in the Andes? *Geology*, *33*(8),  
818 617–620. <https://doi.org/10.1130/G21557AR.1>.
- 819 Sobolev, S. V., Babeyko, A. Y., Koulakov, I., & Oncken, O. (2006). Mechanism of the  
820 Andean Orogeny: Insight from Numerical Modeling. In O. Oncken, G. Chong, G.  
821 Franz, P. Giese, H.-J. Götze, V. A. Ramos, et al. (Eds.), *The Andes* (pp. 513–535).  
822 Springer Berlin Heidelberg. [https://doi.org/10.1007/978-3-540-48684-8\\_25](https://doi.org/10.1007/978-3-540-48684-8_25).
- 823 Spencer, J. E. (1996). Uplift of the Colorado Plateau due to lithosphere attenuation during  
824 Laramide low-angle subduction. *Journal of Geophysical Research: Solid Earth*,  
825 *101*(B6), 13595–13609. <https://doi.org/10.1029/96JB00818>.
- 826 Stockmal, G. S., Beaumont, C., Nguyen, M., & Lee, B. (2007). Mechanics of thin-skinned  
827 fold-and-thrust belts: Insights from numerical models. *Geological Society of America*  
828 *Special Papers*, *433*, 63–98. [https://doi.org/10.1130/2007.2433\(04\)](https://doi.org/10.1130/2007.2433(04)).
- 829 Strecker, M. R., Alonso, R. N., Bookhagen, B., Carrapa, B., Hilley, G. E., Sobel, E. R., &  
830 Trauth, M. H. (2007). Tectonics and Climate of the Southern Central Andes. *Annual*  
831 *Review of Earth and Planetary Sciences*, *35*(1), 747–787.  
832 <https://doi.org/10.1146/annurev.earth.35.031306.140158>.
- 833 Tassara, A., Götze, H.-J., Schmidt, S., & Hackney, R. (2006). Three-dimensional density  
834 model of the Nazca plate and the Andean continental margin. *Journal of Geophysical*  
835 *Research: Solid Earth*, *111*(B9). <https://doi.org/10.1029/2005JB003976>.
- 836 Tesauro, M., Kaban, M. K., & Cloetingh, S. A. P. L. (2013). Global model for the lithospheric  
837 strength and effective elastic thickness. *Tectonophysics*, *602*, 78–86.  
838 <https://doi.org/10.1016/j.tecto.2013.01.006>.
- 839 Whitman, D., Isacks, B. L., & Kay, S. M. (1996). Lithospheric structure and along-strike  
840 segmentation of the Central Andean Plateau: seismic Q, magmatism, flexure,  
841 topography and tectonics. *Tectonophysics*, *259*(1–3), 29–40.  
842 [https://doi.org/10.1016/0040-1951\(95\)00130-1](https://doi.org/10.1016/0040-1951(95)00130-1).
- 843 Yonkee, W. A., & Weil, A. B. (2015). Tectonic evolution of the Sevier and Laramide belts  
844 within the North American Cordillera orogenic system. *Earth-Science Reviews*, *150*,  
845 531–593. <https://doi.org/10.1016/j.earscirev.2015.08.001>.
- 846 Yuan, X., Sobolev, S. V., & Kind, R. (2002). Moho topography in the central Andes and its  
847 geodynamic implications. *Earth and Planetary Science Letters*, *199*(3–4), 389–402.  
848 [https://doi.org/10.1016/S0012-821X\(02\)00589-7](https://doi.org/10.1016/S0012-821X(02)00589-7).

849

850

851 **Figure 1.** Initial model geometry with thermal-mechanical boundary conditions. The prescribed  
852 compression velocity ( $V_R$ ) from the right-hand side boundary is balanced by the uniform outflux  
853 velocity ( $V_L$ ) along the left-hand side boundary under the orogenic lithosphere. Orange line is the  
854 initial thermal field. The temperature of the lithosphere-asthenosphere boundary ( $T_{LAB}$ ) varies between  
855 1324 °C and 1380 °C, depending on the lithospheric thickness. The crustal thickness in the orogen  
856 ( $H_{oc}$ ) varies from 36 km to 70 km. The lithospheric thicknesses of the orogen ( $H_{ol}$ ) and the  
857 foreland ( $H_{fl}$ ) vary from 60 km to 200 km. The thickness of the foreland sediment ( $H_{se}$ ) varies from  
858 0 to 8 km, and the value of its friction coefficient ( $\mu_{se}$ ) is between 0.5 and 0.02. The white dashed  
859 line is the boundary between the orogen and its foreland. Qtz<sub>wet</sub>, MD<sub>dry</sub>, and Ol<sub>dry</sub> in the example of the  
860 60-km-thick lithospheric strength profile indicate wet quartzite, dry Maryland diabase, and dry olivine,  
861 respectively.

862

863 **Figure 2.** Reference Model M1. **a)** Lithospheric strength profiles of the orogen (left) and its foreland  
864 (right). **b)** and **c)** are model profiles of the phase and the deformation pattern after 100 km shortening,  
865 respectively. The two small bars above the phase profile are lithospheric structures of the orogen and  
866 its foreland. The value of the lithospheric thickness (white) is inside them. The black line is the  
867 boundary between material phases. The black dashed line with two arrows represents the thick-  
868 skinned tectonics in the foreland.

869

870 **Figure 3.** Foreland deformation patterns for some selected models in **Table 2** after 100 km  
871 shortening, showing **a-e)** effects of individual factors and **f-j)** effects of multiple factors. Foreland  
872 sediments (the red part in the structure bar of the foreland lithosphere) are considered initially weak  
873 when its thickness is greater than 4 km and its friction coefficient is not higher than 0.05. The black  
874 solid line with two arrows represents the tectonic style of thin-skinned in the foreland.

875

876 **Figure 4.** Foreland deformation patterns **a, c)** without or **b, d)** with weak foreland sediments. The  
877 orogen is weaker than the foreland when the strength ratio is smaller than 1. Four different tectonic  
878 styles are fully thick-skinned (dark blue), thick-skinned dominated (light blue), thin- and thick-skinned  
879 mixed (red), and fully thin-skinned (green). The gray dashed curve shows the presumptive transition  
880 between pure- and simple-shear shortening modes. Hollow stars indicate four natural examples with  
881 different foreland deformation patterns. R.M. - Rocky Mountains; S.P. - Sierras Pampeanas.

882

883 **Figure. 5.** Numerical models applied to the Central-Southern Andes and Southern Rocky Mountains.  
884 **a)** is a simplified tectonic map modified from Kay & Coira (2009). The tan area shows the elevation  
885 above 3.7 km. The geological structures of transects A-A' and B-B' modified from Kley et al. (1999)  
886 show **b)** fully thin-skinned tectonics in the Interandean-Subandean zone and **c)** fully thick-skinned

887 tectonics in the Santa Barbara system. Transect C-C', which is modified from Siame et al. (2006),  
 888 Bellahsen et al. (2016), and Mescua et al. (2016), shows **d**) the thin- and thick-skinned mixed tectonic  
 889 style in the Precordillera-Sierras Pampeanas system. **e**) Tectonic map of the Colorado Plateau and  
 890 Southern Rocky Mountain foreland, based on Liu & Currie (2016) and reference therein. **f**) The  
 891 geological structure of transect D-D', modified from Lacombe & Bellahsen (2016) and Yonkee &  
 892 Weil (2015), and its modeled foreland deformation pattern.

893

894 **Figure A1.** The list of initial lithospheric strength curves with different initial lithospheric structures  
 895 (60-200 km) and crustal structures (36-60 km), showing lithospheric strengths of the orogen and its  
 896 foreland for each of the aforementioned model in **Table 2**. For example, M1-M5: Foreland, means that  
 897 models M1-M5 contain an initial 100-km-thick lithosphere in the foreland. M2, M12: Orogen, means  
 898 that in M2 and M12, the initial thickness of the orogenic lithosphere is 60 km and its crust is 36 km  
 899 thick.

900

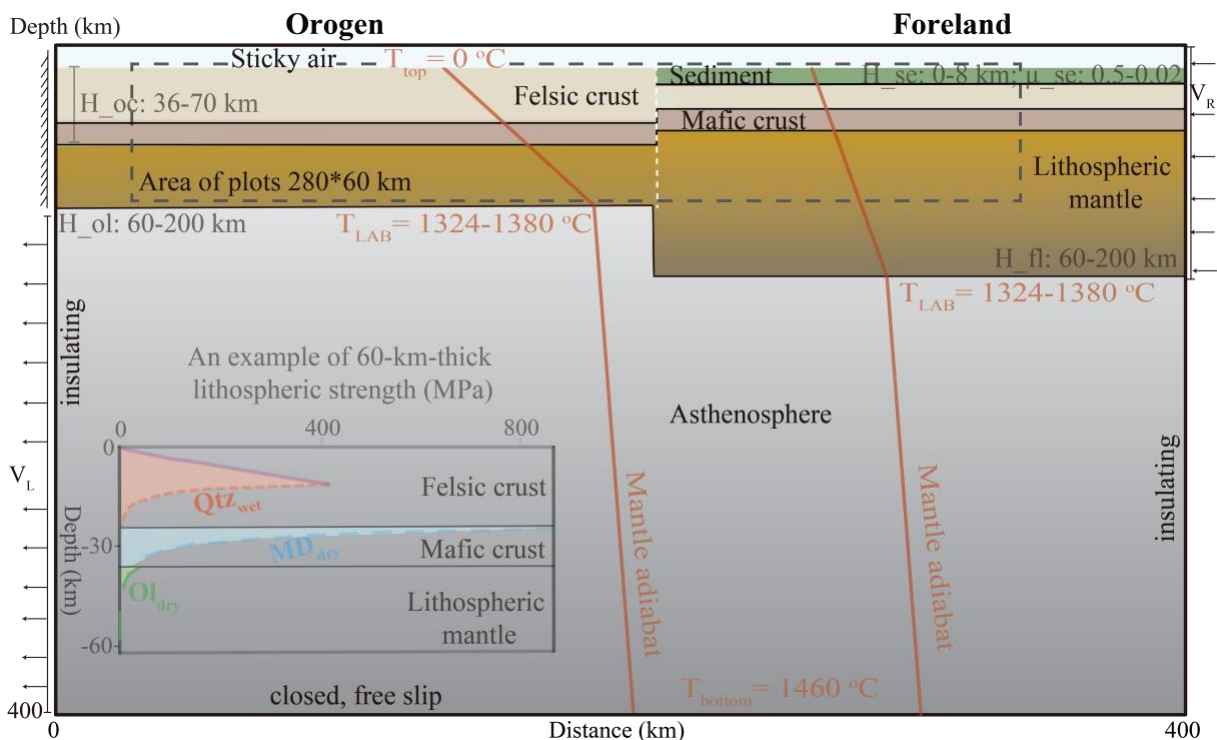
901 **Table 1** Material properties in the numerical models

902

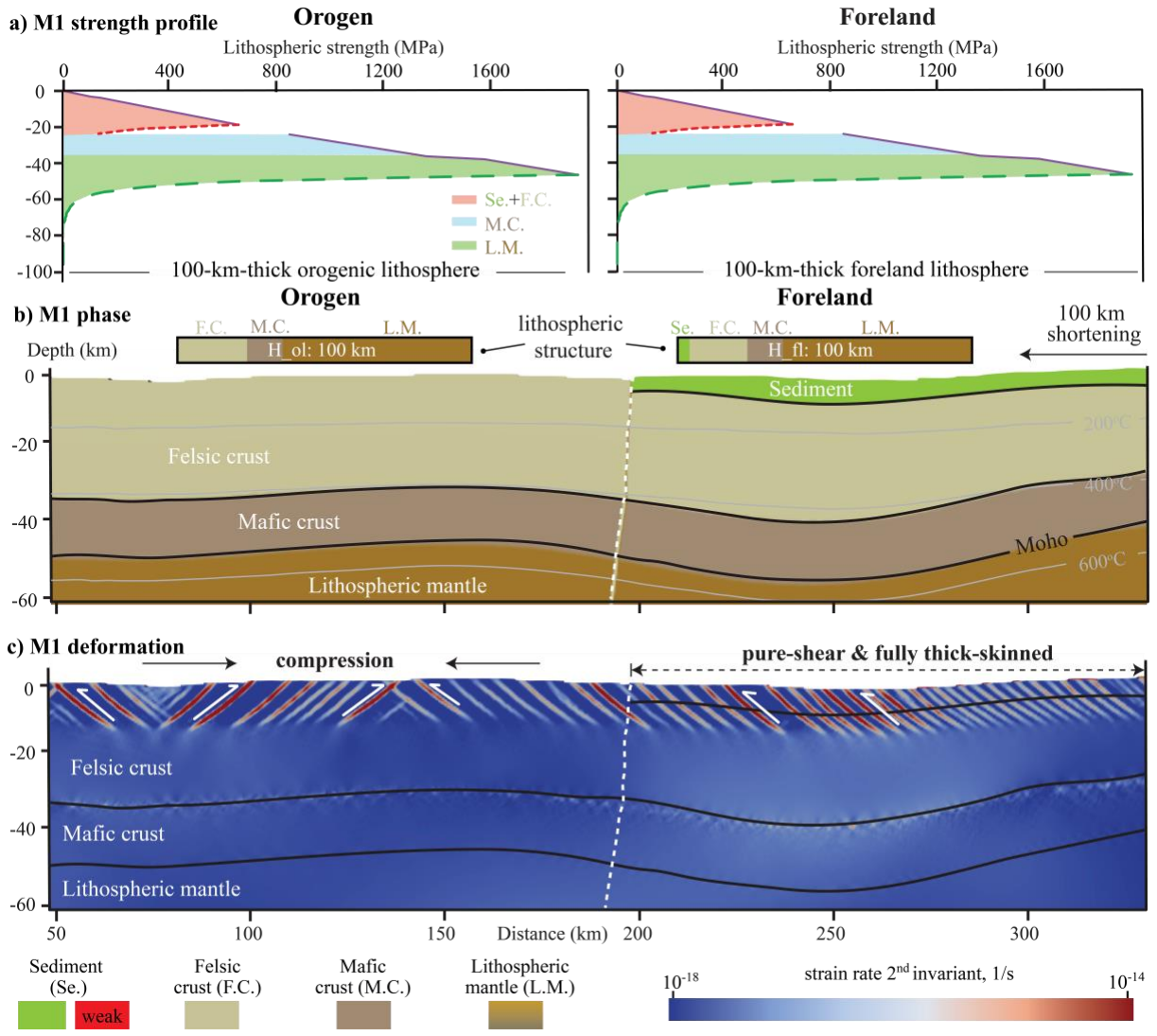
903 **Table 2** The list of the orogen-foreland shortening models.  $H_{ol}$ : thickness of the orogenic  
 904 lithosphere,  $H_{fl}$ : thickness of the foreland lithosphere,  $H_{oc}$ : thickness of the orogenic crust,  $H_{se}$ :  
 905 thickness of foreland sediments,  $\mu_{se}$ : friction coefficient of foreland sediments; S. mode: shortening  
 906 mode, S-1: pure-shear, S-2: simple-shear; T. style: tectonic style, T-1: fully thick-skinned, T-2: thick-  
 907 skinned dominated, T-3: thin- and thick-skinned mixed, T-4: fully thin-skinned.

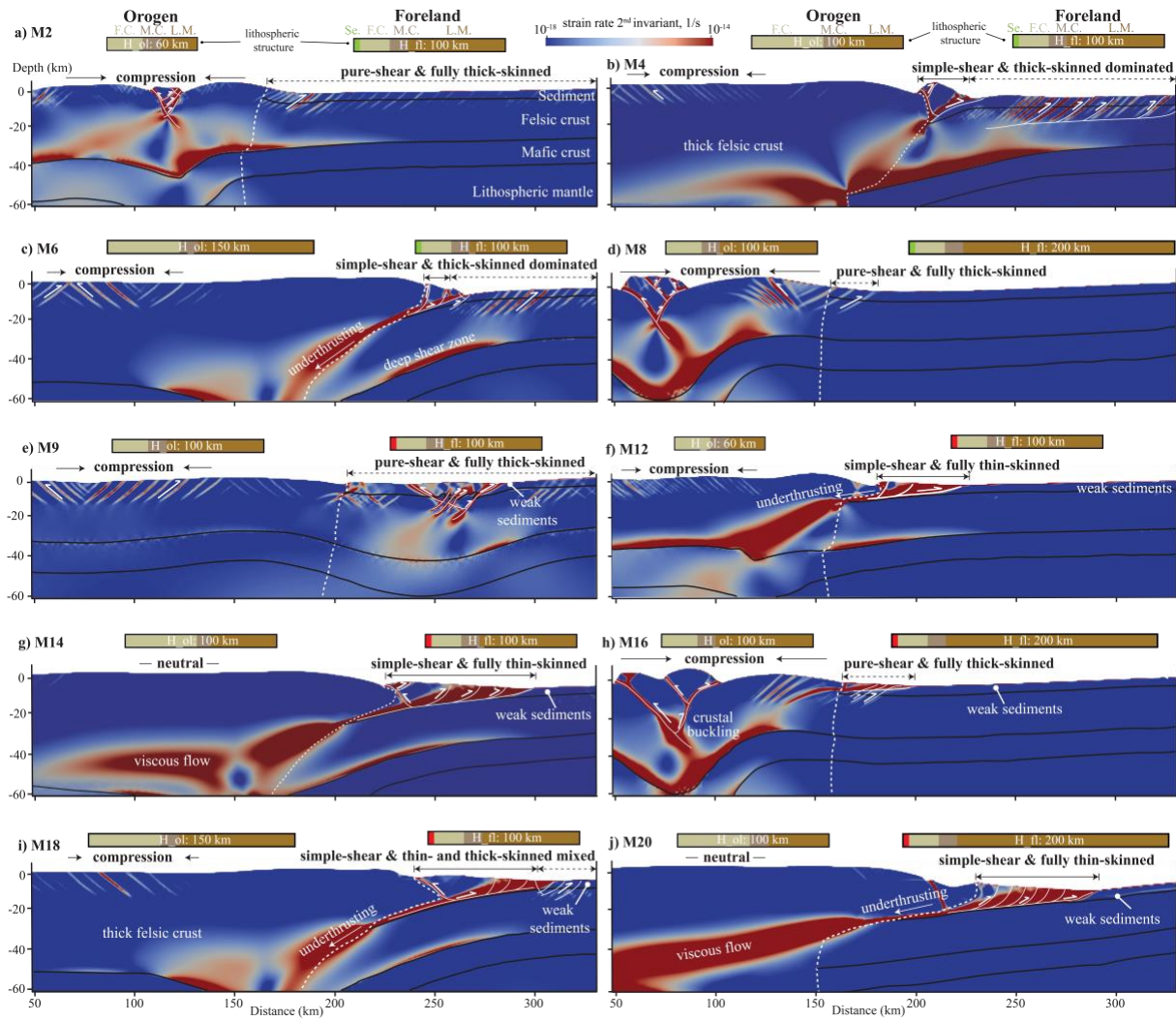
908

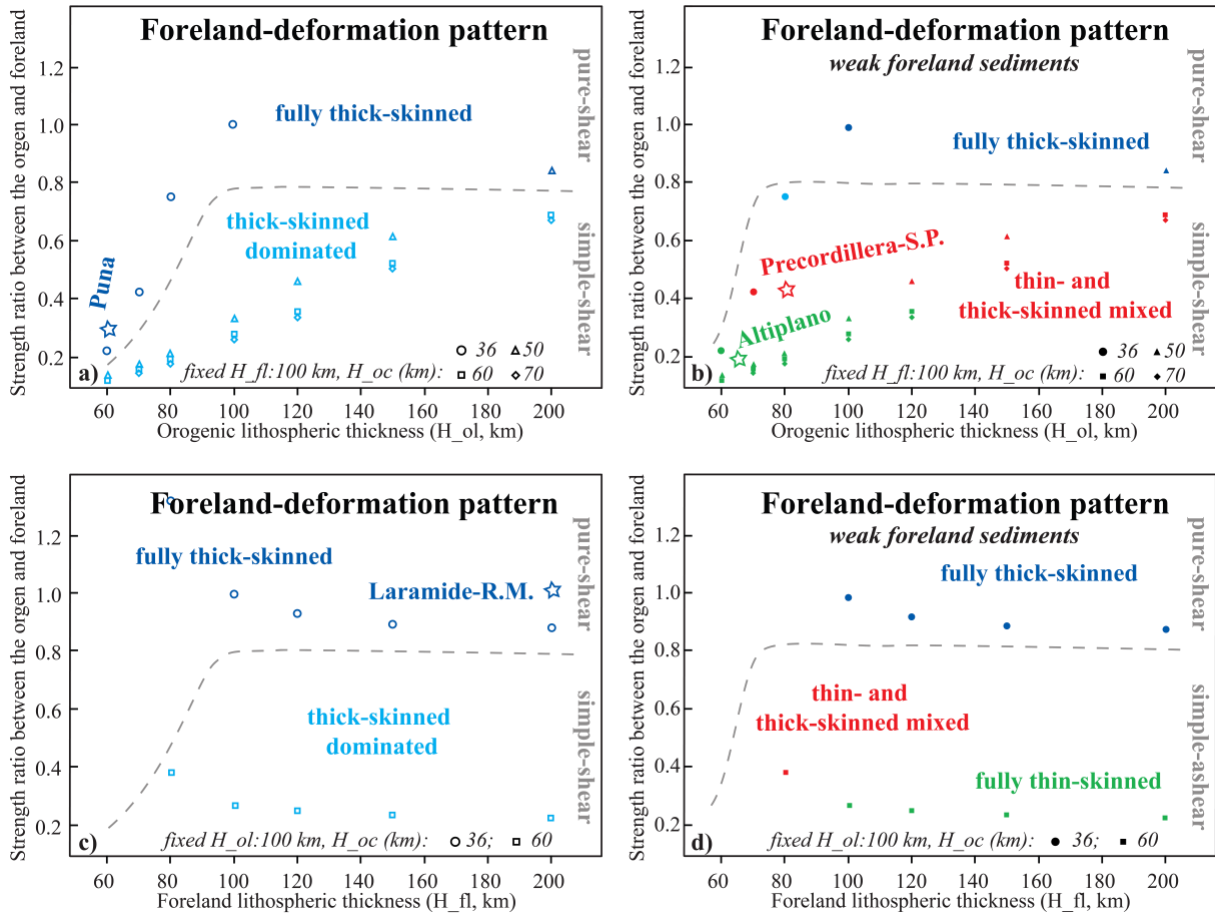
909 **Figure 1**

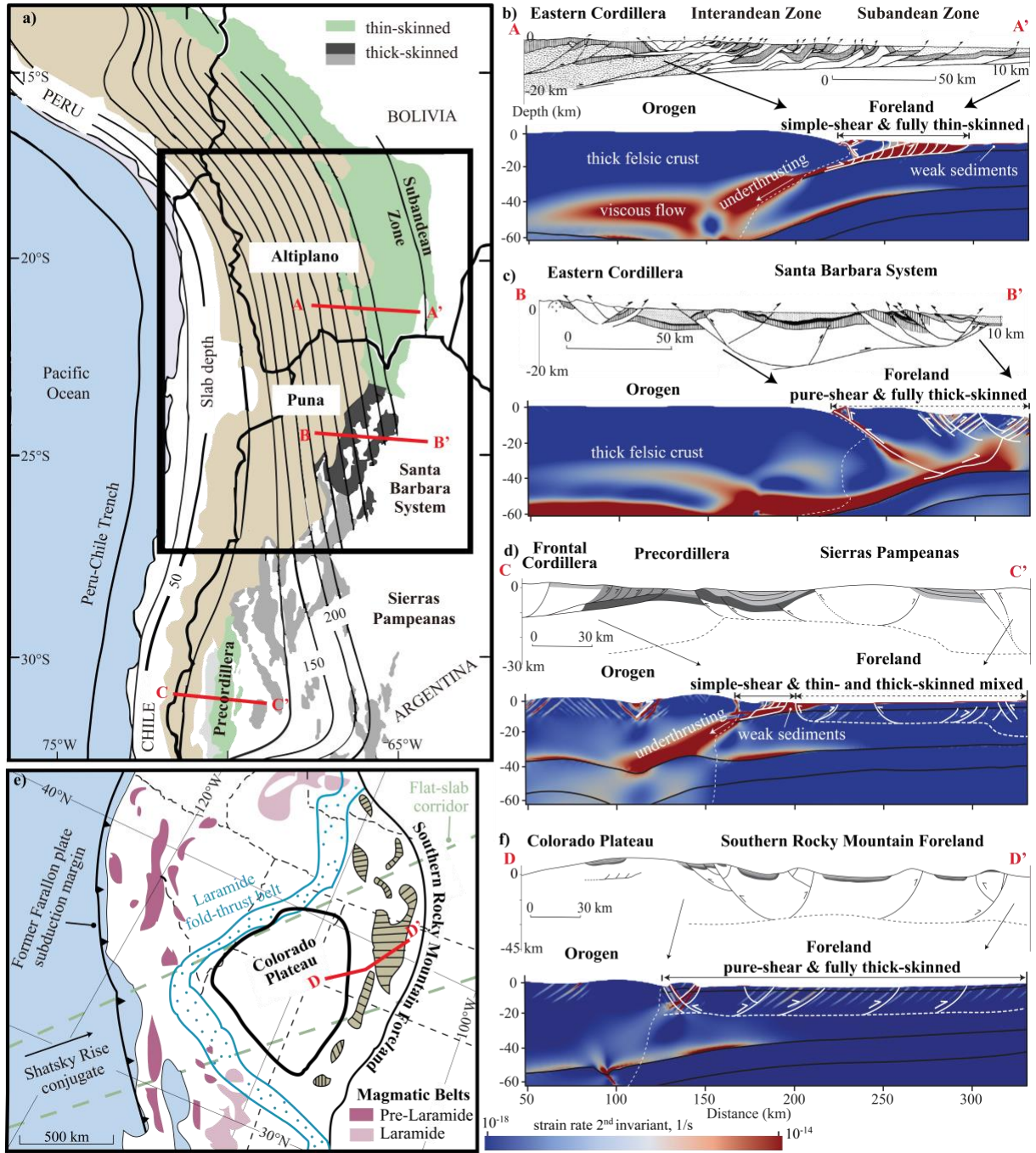


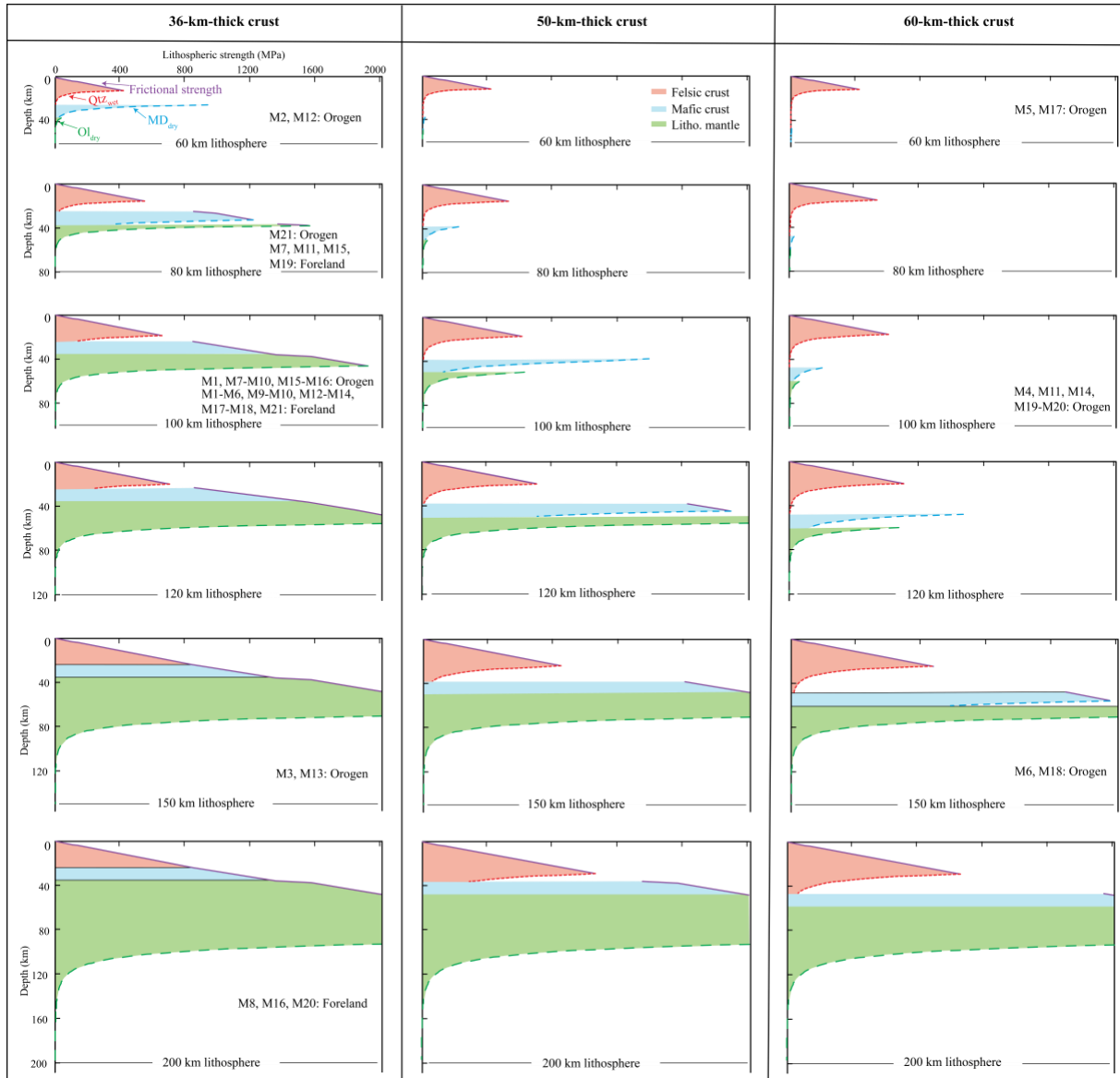
910











Phase	Sediments; Felsic crust	Mafic crust	Lithospheric mantle	Asthenosphere
Density <sup>1</sup> , $\rho_0$ (kg/m <sup>3</sup> )	2500; 2800	3000	3300	3300
Heat expansion, $\alpha$ (K <sup>-1</sup> )	3.7e-5	2.7e-5	3e-5	3e-5
Specific heat, $C_p$ (kJ kg <sup>-1</sup> K <sup>-1</sup> )	1.2	1.2	1.2	1.2
Heat conductivity, $k$ (W K <sup>-1</sup> m <sup>-1</sup> )	2.5	2.5	3.3	3.3
Heat productivity, $A$ ( $\mu$ Wm <sup>-3</sup> )	1.0	0.3	0	0
Friction angle <sup>2</sup> , $\varphi$ (°)	3; 30-6	30	30	30
Cohesion <sup>2</sup> , $C_0$ (MPa)	1; 20-1	40	40	40
Elastic shear modulus, $G$ (GPa)	36	40	74	74
Creep pre-exponential factor <sup>3</sup> , Bf/Bl (Pa <sup>-n</sup> s <sup>-1</sup> )	-/8.57e-28	-/5.78e-27	1.5e-9/ 6.22e-16	1e-9/ 2.03e-15
Creep activation energy <sup>3</sup> , Ef/El (kJ mol <sup>-1</sup> )	-/223	-/485	375/480	335/480
Creep activation volume <sup>3</sup> , Vf/Vl (cm <sup>3</sup> mol <sup>-1</sup> )	-/0	-/0	5/11	4/11
Power law exponent <sup>3</sup> , nf/nl	-/4	-/4.7	1/3.5	1/3.5
<p><sup>1</sup>Initial temperature-dependent density: <math>\rho_{p,T} = \rho_0[1 - \alpha(T - T_0)]</math>, where <math>\rho_0</math> is the reference density at temperature <math>T_0</math>.</p> <p><sup>2</sup>Strain-softening in the felsic crust via a decrease in <math>\varphi</math> and <math>C_0</math> over the accumulated strain of 0.5 to 1.5. Sediment is assumed to be initially weak if it is 4-km-thick and <math>\varphi</math> is 3° and <math>C_0</math> is 1 MPa.</p> <p><sup>3</sup>Viscous creep includes diffusion (Bf, Ef, Vf, nf) and dislocation (Bl, El, Vl, nl).</p>				

Models	Lithospheric thickness (km)		Crustal thickness (km)	Foreland sedimentary strength		Foreland deformation pattern		Fig. #
	H <sub>ol</sub>	H <sub>fl</sub>	H <sub>oc</sub>	H <sub>se</sub>	$\mu_{se}$	S. mode	T. style	
M1	100	100	36	4	0.58	S-1	T-1	2
M2	60	100	36	4	0.58	S-1	T-1	3a
M3	150	100	36	4	0.58	S-1	T-1	
M4	100	100	60	4	0.58	S-2	T-2	3b
M5	60	100	60	4	0.58	S-2	T-2	
M6	150	100	60	4	0.58	S-2	T-2	3c
M7	100	80	36	4	0.58	S-1	T-1	
M8	100	200	36	4	0.58	S-1	T-1	3d
M9	100	100	36	4	0.05	S-1	T-1	3e
M10	100	100	36	8	0.02	S-1	T-1	
M11	100	80	60	4	0.58	S-2	T-2	
M12	60	100	36	4	0.05	S-2	T-4	3f
M13	150	100	36	4	0.05	S-1	T-1	
M14	100	100	60	4	0.05	S-2	T-4	3g
M15	100	80	36	4	0.05	S-1	T-1	
M16	100	200	36	4	0.05	S-1	T-1	3h
M17	60	100	60	4	0.05	S-2	T-4	
M18	150	100	60	4	0.05	S-2	T-3	3i
M19	100	80	60	4	0.05	S-2	T-3	
M20	100	200	60	4	0.05	S-2	T-4	3j

**Controls of the Foreland Deformation Pattern in the Orogen-Foreland Shortening System: Constraints from High-Resolution Geodynamic Models**

Sibiao Liu<sup>1, 2, 3</sup>, Stephan V. Sobolev<sup>2, 3</sup>, Andrey Y. Babeyko<sup>2</sup>, Michael Pons<sup>2, 3</sup>

<sup>1</sup>GEOMAR Helmholtz Centre for Ocean Research Kiel, Kiel, Germany

<sup>2</sup>German Research Center for Geosciences GFZ, Potsdam, Germany

<sup>3</sup>Institute of Earth and Environmental Science, University of Potsdam, Potsdam, Germany

**Contents of this file**

Figures S1 and S2

**Introduction**

This document contains four supplementary figures. Figure S1 encapsulates a series of modeling experiments that we conducted and is a supplement to Table 2 in the main text. Figure S2 show model results of the full-size models M2 undergoing 178 km of shortening.

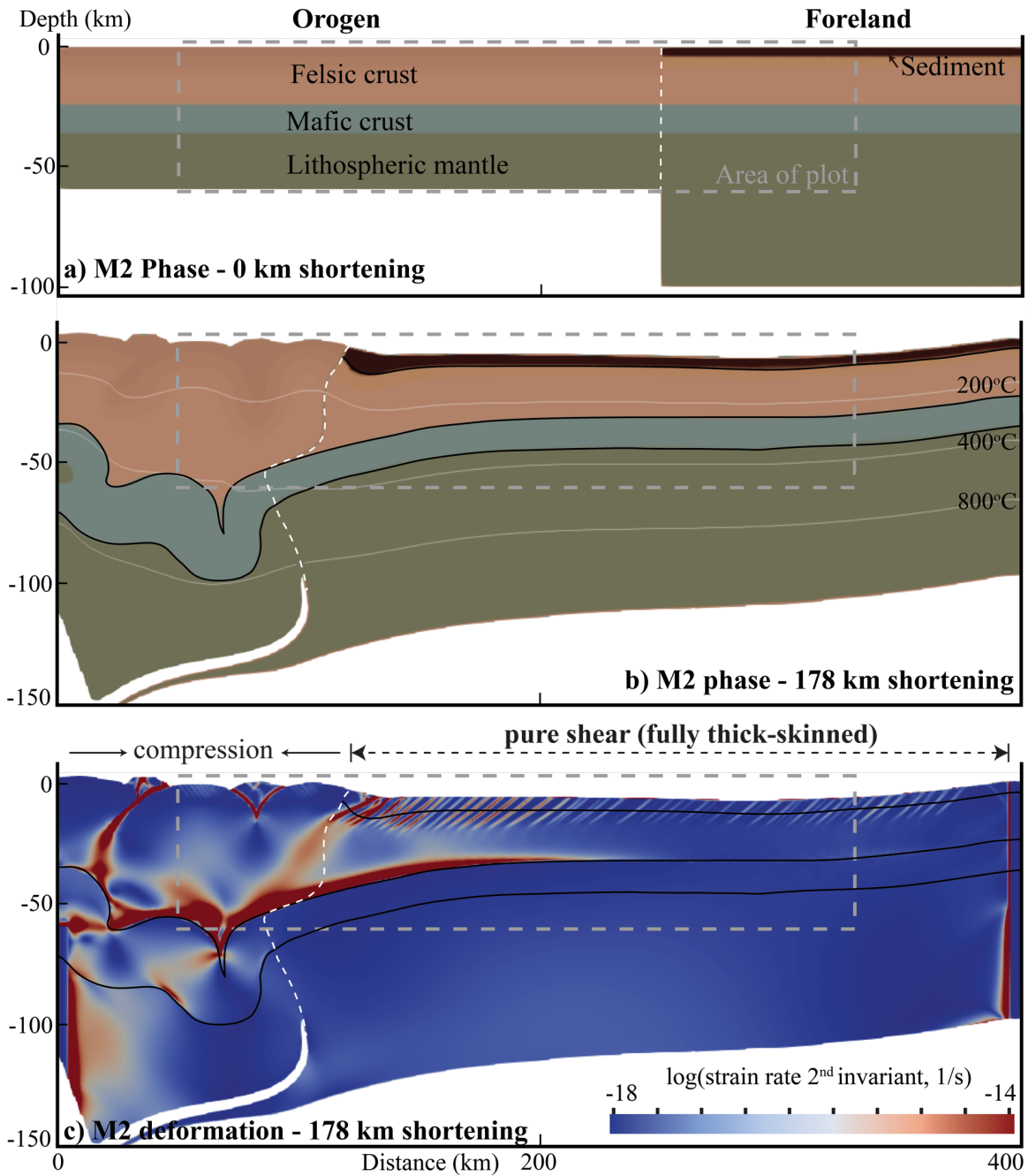


**Figure S1.** Results of Model M2 after 178 km of shortening. **a)** Initial model setup. **b)** and **c)** are model profiles of the phase and deformation structure, respectively.

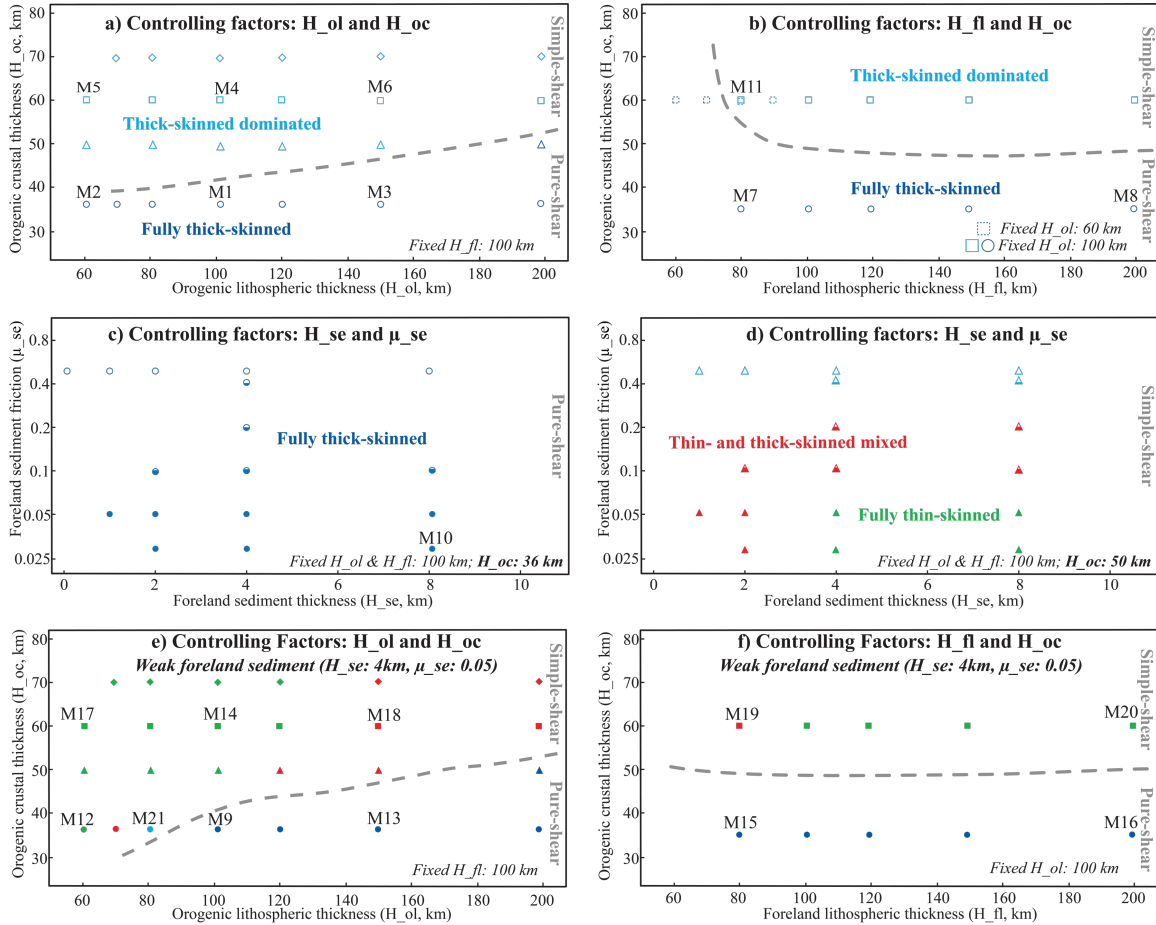


**Figure S2.** Model behaviors for variations in orogenic/foreland lithospheric thickness, orogenic crustal thickness, and foreland sedimentary thickness and friction coefficient. **a-b)** Models with controlling factors: thickness of the orogenic lithosphere ( $H_{ol}$ ) and thickness of the orogenic crust ( $H_{oc}$ ). Thickness of the foreland lithosphere ( $H_{fl}$ ) is fixed. **c-d)** Models with controlling factors: thickness of the foreland sediment ( $H_{se}$ ) and its friction coefficient ( $\mu_{se}$ ).  $H_{oc}$  and  $H_{fl}$  are fixed.  $H_{oc}$  are 36 km and 50 km in **c)** and **d)**, respectively. **e-f)** Models have the same factors as **a-b)** except an additional weak foreland sedimentary layer. The gray dashed curve shows the presumptive transition between two shortening modes.